

To appear in *The Astrophysical Journal*

Effects of Dust Growth and Settling in T Tauri Disks

Paola D'Alessio¹, Nuria Calvet², Lee Hartmann², Ramiro Franco-Hernández^{1,3}, and Hermelinda Servín¹

Electronic mail: p.dalessio@astrosmo.unam.mx, ncalvet@umich.edu,
lhartm@umich.edu, r.franco@astrosmo.unam.mx

ABSTRACT

We present self-consistent disk models for T Tauri stars which include a parameterized treatment of dust settling and grain growth, building on techniques developed in a series of papers by D'Alessio et al. . The models incorporate depleted distributions of dust in upper disk layers along with larger-sized particles near the disk midplane, as expected theoretically and as we suggested earlier is necessary to account for mm-wave emission, SEDs, scattered light images, and silicate emission features simultaneously. By comparing the models with recent mid- and near-IR observations, we find that the dust to gas mass ratio of small grains at the upper layers should be $< 10\%$ of the standard value. The grains that have disappeared from the upper layers increase the dust to gas mass ratio of the disk interior; if those grains grow to maximum sizes of the order of mm during the settling process, then both the millimeter-wave fluxes and spectral slopes can be consistently explained. Depletion and growth of grains can also enhance the ionization of upper layers, enhancing the possibility of the magnetorotational instability for driving disk accretion.

Subject headings: Accretion, accretion disks, Stars: Circumstellar Matter, Stars: Formation, Stars: Pre-Main Sequence

¹Centro de Radioastronomía y Astrofísica, Ap.P. 72-3 (Xangari), 58089 Morelia, Michoacán, México

²Dept. of Astronomy, University of Michigan, 825 Dennison Building, 500 Church St., Ann Arbor, MI 48109, USA

³Harvard-Smithsonian Center for Astrophysics, 60 Garden St., Cambridge, MA 02138, USA.

1. Introduction

It is commonly accepted that disks around T Tauri stars are mostly heated by stellar radiation intercepted by the flared surfaces of these disks (Kenyon & Hartmann 1987; 1995). A large fraction of the intercepted radiation is deposited in the disk upper atmosphere, which becomes hotter than deeper layers, producing spectral features in emission such as the observed silicate bands (Calvet et al. 1991, 1992; Chiang & Goldreich 1997; D’Alessio et al. 1998; Natta, Meyer & Beckwith 2000). Stellar radiation is absorbed by dust grains in the disk, which reemit the energy at longer wavelengths. Analyses of the spectral energy distributions (SEDs) combined with disk structure calculations thus provide information on the properties and state of the solid particles in the disk.

The flat slopes of the SEDs at mm wavelengths, indicative of grains larger than those in the ISM, have suggested dust evolution in T Tauri disks for some time (Beckwith et al. 1990; Beckwith & Sargent 1991; Miyake & Nakagawa 1993; Pollack et al 1994 = P94). Interpretation of scattered light images in the optical and near IR provide additional evidence for grain growth (Cotera et al. 2001; D’Alessio et al. 2001; Watson & Stapelfeldt 2004).

In a series of papers (D’Alessio et al. 1998, 1999b, 2001; Papers I, II, and III, respectively), we have developed physically self-consistent models of T Tauri accretion disks and explored observational predictions based on these models. They include both viscous dissipation and heating by irradiation from the central star. The disk structure is solved iteratively, as the vertical disk thickness depends upon the irradiation heating, which in turn depends upon the vertical structure. Changes in the dust opacity affect the vertical disk structure and therefore the temperature and density distribution as a function of both radius and height.

In Paper II we showed that models in which the disk has dust like that inferred for the diffuse interstellar medium (ISM) (i.e., silicates and graphite grains, with abundances and optical properties from Draine & Lee (1984 = DL) and a maximum grain radius $a_{max} \sim 0.25 \mu m$) uniformly mixed with the disk gas (*well mixed models*), fail to explain detailed observations. Specifically, the models exhibit too little mm-wave emission and larger far-infrared fluxes than observed from typical CTTS for reasonable disk masses; the models are too geometrically thick in the direction perpendicular to the midplane, which results in wider dark lanes in scattered light images of edge-on disks than observed; and the models predict too large a fraction of stars extinguished by their disks than observed in surveys, assuming a random distribution of inclinations.

Motivated by the need to improve the agreement with observations, in Paper III we considered the effects of changing dust properties in well-mixed models. We showed that

well mixed models in which dust grain radii (a) follow a power-law distribution $n(a) \propto a^{-p}$, $2.5 \leq p \leq 3.5$, with a maximum grain radius ~ 1 mm, can explain the above observational constraints. Grains bigger than typical ISM dust grains affect both the long- and short-wavelength predicted properties of the dust mixture; larger grains yield a larger mm-wave emissivity and spectral indices in better agreement with observations. At the same time, the number of small grains is reduced to account for the mass locked up in large grains, and this decreases the optical and near-infrared opacity. This results in less absorption of stellar flux, lower disk temperatures, and a decreased IR emission. Similarly, the predicted dark-lanes in scattered light images of edge-on disks are narrower, and the expected number of heavily extincted stars becomes consistent with observations. However, since big grains have a gray opacity at wavelengths much shorter than their sizes, such disk models predict **no silicate emission bands**, while these features are ubiquitous in T Tauri disks (Cohen & Wittborn 1985; Natta et al. 2000), and as strongly confirmed by large surveys using the Infrared Spectrograph on the *Spitzer* Space Telescope (Forrest et al. 2004; Furlan et al. 2005a,b).

Grain evolution is predicted by solar nebula models, in which solid particles are found to grow and settle to the midplane, making planetesimals and ultimately leading to planetary formation (Weidenschilling & Cuzzi 1993, and references therein; Weidenschilling 1997; Dullemond & Dominik 2004b). In such models the upper layers of the disk are rapidly depleted of dusty material, and only the smallest grains extend to larger vertical heights in the disk, because the largest grains settle more quickly. Grain growth and settling provide an explanation for the observed SEDs, because small grains populate the upper layers and produce conspicuous emission dust features, but at the same time the reduced number of small grains lowers the optical and near-infrared opacities, while creating a population of large particles in the disk interior consistent with high long-wavelength emission (§2.1).

Following these suggestions, Chiang et al. (2001) explored a two layer disk model with small grains ($a_{max} \sim 1 \mu m$) in the upper hot layer and larger grains ($a_{max} \sim 1$ mm) in the disk interior, and obtained SEDs with conspicuous silicate and water ice bands and high mm emission. In their model, the *irradiation surface*, that is, the surface where the optical depth to the stellar radiation is unity, was taken to be some free parameter times the interior gas scale height. However, if the irradiation surface had been self-consistently calculated, it would have been similar to the one calculated in a well mixed disk with small dust, because the optical depth to the stellar radiation is built in the uppermost layers, which in their models had a standard abundance of small grains.

More recently, Dullemond & Dominik (2004b) followed the evolution of dust grains as they settled in the disk and calculated the SEDs along this evolution. They showed the main

effects of dust evolution of the SEDs, namely, that the IR fluxes decrease as the degree of settling increases. However, although theories of dust settling make detailed predictions for the distribution and evolution of dust properties in the disk, they fail to predict time scales consistent with observations. Weidenschilling (1997) and Dullemond & Dominik (2004b) predicted that disks reach a large degree of dust settling in less than 1 Myr years, while CTTS with flared outer disks are present, in the Taurus population, with ages of 1 - 2 Myr (Hartmann 2003) as well as in the 10 Myr old TW Hya association (Calvet et al. 2002). Dullemond & Dominik (2004, 2005) suggested several possibilities to overcome this problem. One suggestion was that this might be a selection effect, but studies of the IRAS sources in Taurus (Kenyon et al. 1990) are fairly complete (see discussion in Paper II). Dullemond & Dominik also suggested that other factors such as different degrees of turbulence, grain properties and shapes, uncertain sticking probabilities and other incompleteness in the treatment of settling may explain the long lifetimes of small dust at high disk altitudes.

In view of these problems, we take a parameterized approach in this paper to describe the effects of settling. We parameterize the dust properties and distributions, and calculate the resultant disk structure and emission, using our treatment of irradiated accretion disks. Unlike other studies, we obtain a surface density distribution which is consistent with the mass accretion rate and the temperature structure resultant from the adopted dust distribution. Comparison with observations will indicate the range of parameters that best characterize populations at given age, putting constraints into the uncertain parameters in the physical description of grain growth and settling in protoplanetary disks.

Specifically, we consider disk models with two populations of dust grains with different spatial distributions in the disk and different dust to gas mass ratios, small grains in the upper levels, large grains in the midplane. We explore the effect on the disk structure and SED of changing the dust to gas mass ratio in both populations consistently (§3). By comparing to observations, specially results from the Spitzer mission, these predictions will help to place constraints on the amount of dust growth and settling (§4). We close by considering the implications of our results for dust growth models and for the ionization state of T Tauri disks, a critical issue in determining the possible role of the magneto-rotational instability in driving accretion (§5).

2. General considerations

2.1. Overview

The situation we are considering is illustrated schematically in Figure 1 (see also Papers I-III; Chiang & Goldreich 1997). Disk heating (at most radii) is dominated by the absorption of light from the central star. This radiation is absorbed in the upper, low-density layers of the disk (the *absorption layers*), because of the large dust opacity at the short wavelengths characteristic of the stellar emission and the impinging angle of this incident radiation. The absorbed stellar light is re-radiated at longer wavelengths; about half of this emission enters into deeper layers of the disk (e.g. Chiang & Goldreich 1997). We define an irradiation surface $z_s(R)$ such that the mean optical depth integrated along the radial direction to the star is unity. The amount of stellar flux entering the disk at a fixed R is approximately proportional to μ_0 , which is the cosine of the angle between the radial direction and the local normal to the surface defined by $z_s(R)$. Thus, the shape of $z_s(R)$, i.e., μ_0 , determines the input energy and thus the principal heating at most radii.

The characteristic opacity to the stellar radiation in the upper layers is the key agent in heating of the disk. If the deeper layers of the disk are optically thick to their own characteristic wavelengths of radiation, the resulting continuum emission is mostly controlled by the amount of heating due to absorption of stellar light, and therefore it is mostly determined by the opacity in the upper disk layers. The IR continuum radiation emerging from optically thick annuli of the disk is characteristic of the *photospheric height*, z_{phot} , where the Rosseland mean vertical optical depth is $\tau_R(z) = 2/3$. When the disk deeper layers are optically thin to their own characteristic wavelength of radiation (i.e., the total vertical optical depth is $\tau_R < 2/3$), the disk interior becomes vertically isothermal; it is heated by the stellar radiation reprocessed by the upper layers and it cools down by emission at longer wavelengths emerging from every layer. Thus, the temperature in the outer disk, depends on both the short-wavelength opacity in the upper disk layers and the longer wavelength opacity in the deeper layers.

The emissivity as a function of wavelength of the upper optically thin layers, heated by direct stellar radiation, depends on their dust content. Small grains have much higher opacities in the stellar radiation wavelength range than large grains; thus, disks with small grains have steeper irradiation surfaces and higher temperatures than disks with large grains; thus, disks with small grains have steeper irradiation surfaces and higher temperatures than disks with large grains. Grain growth can be inferred not only from the slope and strength of the millimeter flux, but from the overall level of the IR fluxes. Using these properties, we determined that the median fluxes of Taurus were consistent with a relatively low stellar

absorption, as that due to large grains, $a_{max} = 1$ mm, rather than to the higher absorption of the smaller ISM dust (paper III).

Small grains will show spectral features that disappear when there is a significant fraction of big grains characterized by a more nearly gray opacity. For instance, the $10 \mu m$ silicate band is present for a dust size distribution given by a power law, $n(a) \sim a^{-3.5}$ between a minimum grain size $a_{min} = 0.005 \mu m$ and a maximum grain size $a_{max} < 1 \mu m$, but it tends to disappear for a much larger maximum size (see paper III). Thus, the well mixed model that fitted the median SED of Taurus could not produce the silicate emission, ubiquitous in T Tauri disks.

Dust growth and settling results in spatially different distributions of grain sizes and abundances. Starting with a uniform distribution in the disk, larger particles begin to settle toward the midplane, leaving behind a population of small grains with a lower dust to gas mass ratio (Weidenschilling 1997; Dullemond & Dominik 2004b). This size-dependent settling has distinct effects on the spectral energy distribution, which can be illustrated with the following approximate description.

The emergent intensity of the optically thin upper layers is given approximately by (e.g., Natta, et al. 2000),

$$I_{\nu}^{thin} \approx B_{\nu}(T_0)\kappa_{\nu}\mu_0/\chi_*, \quad (1)$$

where B_{ν} is the Planck function at the characteristic temperature T_0 of the layer, κ_{ν} is the dust true absorption at frequency ν , and χ_* is the Planck mean opacity of the dust evaluated at the stellar effective temperature T_* (calculated integrating the monochromatic total opacity over frequency using $B_{\nu}(T_*)$ as the weighting function). The temperature T_0 at radius R can be estimated assuming that the dust is in radiative equilibrium with the stellar radiation field, i.e.,

$$T_0(R) \approx 0.8[\kappa_*/\kappa_P(T_0)]^{1/4}(R_*/R)^{1/2}T_*, \quad (2)$$

where κ_* and $\kappa_P(T_0)$ are Planck mean true absorptions evaluated at the stellar effective temperature and the local characteristic temperature, respectively, and R_* is the stellar radius. The factor 0.8 in equation (2) accounts for the fact that most of the emission of the layer emerges from a depth close to z_s (see Fig. 1), where the incident stellar radiation that heats the dust has been attenuated.

The approximate equations (1) and (2) show that the temperature and spectrum of the upper layers will change with the wavelength dependence of the opacity but not with the dust to gas mass ratio, since they both depend on opacity ratios [namely κ_{ν}/χ_* and $\kappa_*/\kappa_P(T_0)$]. On the other hand, lowering the dust to gas mass ratio in the upper layers,

decreases their opacity at the stellar radiation, making $z_s(R)$ flatter and μ_0 smaller. These considerations suggest that a model with small grains at the upper layers, with a smaller dust to gas mass ratio in those layers such that the disk roughly has the same surface $z_s(R)$ than the well mixed model with $a_{max} = 1$ mm should be able to explain both, the median SED and the observed 10 μm -silicate band in emission. More generally, the observed SEDs and, in particular, the mid-IR spectral range, can be used to quantify the spatial distribution of the dust in the disks around CTTS, and thus the degree of dust settling toward the midplane.

2.2. Settled disk Models

We construct self-consistent viscous steady irradiated disk models with dust settling. To describe the disk turbulent viscosity, we use the α prescription (Shakura & Sunyaev 1973), i.e., the viscosity coefficient is taken to be $\nu_t = \alpha c_s H$, where c_s and H are the local sound speed and gas scale height, respectively, and α is a free parameter, assumed to be constant throughout the disk. These are irradiated α -disk models.

We have included dust settling in a simple way. For each dust ingredient, we adopt a grain size distribution given by a power law of the grain radius, $n(a) = n_0 a^{-p}$, between a minimum and maximum radius (a_{min} and a_{max}), with an exponent p . The constant n_0 is related to the dust to gas mass ratio ζ of the particular ingredient, the grain bulk density, the minimum and maximum sizes, and p (see Appendix). We explore *settled* disk models with two populations of grains with different size distributions. We describe in detail models in which the *big grains* component has $a_{min} = 0.005 \mu m$, $a_{max} = 1$ mm, $p = 3.5$, and the *small grains* component, $a_{min} = 0.005 \mu m$, $a_{max} = 0.25 \mu m$, $p = 3.5$, and in §3.5 we discuss the effect of changing the small grains maximum size. Both populations have different spatial distributions and dust to gas mass ratios, ζ , i.e., the big grains are concentrated close to the midplane and ζ_{big} may be larger than the standard value because this population incorporates the mass of the dust that has settled from upper layers; the small grains are well mixed with the gas in the rest of the disk, having a lower ζ_{small} than the standard value (i.e., the small grains are depleted). This is an attempt to model in a simple way the complex outcome from detailed studies of the growth of disk dust grains.

In these exploratory calculations, we reduce the parameter space by considering that the big grains are concentrated in the midplane, below a fixed height $z_{big} = 0.1 H$, where H is the local gas scale height. The precise value of z_{big} is arbitrary; we make it small with respect to H to simplify matters. As shown schematically in Figure 1, the small value of z_{big} assures that the upper layer that absorbs the stellar radiation is in the region with the small grains population. To simplify even more, we assume that the grain size distribution

and dust to gas mass ratio do not change with radius, but only with height, and we take the values of the grain maximum size in both populations to be spatially constant. We decrease the free parameter ζ_{small} and increase ζ_{big} to keep the total dust-to-gas mass ratio at the initial (solar) value. Thus we ignore any possible radial concentrations or depletions of solids (e.g., Youdin & Shu 2002).

The calculation of ζ_{big} as a function of ζ_{small} is described in the Appendix. We quantify the depletion of the small grains relative to the standard dust to gas mass ratio using the parameter

$$\epsilon = \zeta_{small}/\zeta_{std} \quad (3)$$

where ζ_{std} is the standard (initial) dust to gas mass ratio. In §3.6 we describe the effects of changing z_{big} .

An important ingredient of the present models is the dust composition and optical properties. We explore two main compositions, one consistent with the disk dust model proposed by P94 and the other one corresponding to the model proposed by DL for the diffuse ISM, to show the effects of dust content. In a future paper, we will attempt detailed fits to individual spectra to explore the range of dust compositions present in young disks. Table 1 lists the adopted ingredients with their standard fractional abundances, ζ_{std} , and sublimation temperatures. For simplicity, we ignore the dependence of sublimation temperature on gas density and grain size. Figure 2 shows the monochromatic absorption coefficient or true opacity and the total opacity for the dust mixtures adopted and different temperature ranges.

Given the dust composition, the maximum grain sizes and the dust to gas mass ratios, the irradiated accretion disk model is calculated as described in papers I, II and III. The input parameters for the disk structure calculations are the mass, radius and effective temperature of the central star (M_* , R_* and T_*), the disk mass accretion rate \dot{M} , and the viscosity

Table 1. Dust ingredients

composition	ingredient	ζ_{std}	$T_{sub}(K)$
ISM	silicates	0.004	1400
	graphite	0.0025	1200
P94	silicates	0.0034	1400
	organics	0.0041	425
	troilite	0.0008	680
	water ice	0.0056	180

parameter α , assumed both to be constant as a function of distance to the central star, as well as the settling parameter ϵ . The disk structure equations in the vertical direction are solved using an iterative scheme which recalculates the absorption of stellar radiation self-consistently given the disk structure in each step.

Two additional parameters have to be specified to obtain the SED: the inclination angle of the disk axis relative to the line of sight, i , and the disk maximum radius, R_d . The SED is calculated by integrating the transfer equation, including thermal and scattering emissivities, along rays that cover the disk projection in the plane of the sky for a given inclination angle and for each wavelength.

We assume the gas and the dust are in thermal balance even at the uppermost layers, which is a good approximation close to z_s (e.g., Kamp & Dullemond 2004) and is correct at deeper denser layers. This assumption implies that a unique temperature characterizes not only gas and dust, but also each grain, regardless its size or composition. For the temperatures of the disk models, hydrogen is in molecular form except in the midplane of the innermost regions of the high mass accretion rate disks. The adopted assumption breaks down for heights above the midplane larger than z_s . In these low density layers, collisions between gas and dust cannot equalize temperatures of gas and dust (Glassgold et al. 2004) nor temperatures of different grains (Chiang et al. 2001). In particular, the gas temperature in the uppermost levels becomes high enough to dissociate molecules (Aikawa & Herbst 2001; Aikawa et al. 2002; Bergin et al. 2003; Willacy et al. 1998; Willacy & Langer 2000). These effects are essential for analysis of molecular observations or detailed studies of dust features, but are less important for the bulk of dust thermal emission considered in this paper.

We show results for a fiducial set of models, which have typical parameters for the CTTS in Taurus, $M_* = 0.5 M_\odot$, $R_* = 2 R_\odot$, $T_* = 4000$ K, $\dot{M} = 10^{-8} M_\odot \text{ yr}^{-1}$, $\alpha = 0.01$, $R_d = 300$ AU and $i = 50^\circ$. The inclination angle $i = 50^\circ$ (or $\cos i = 0.65$) is adopted instead of the typical angle $i = 60$ ($\cos i = 0.5$), which is the average of $\cos i$ for random disk inclinations; this is an attempt to account for the fact that highly inclined disks would have peculiar SEDs and would not be classified as a CTTS SED (see papers II and III; Chiang & Goldreich 1999; §3.8). We explore in detail the dependence of the structure and emission on ϵ for models with these parameters; in §3.7 and 3.8, we study the dependence of the SED on \dot{M} and inclination.

The disk models include the emission from the wall at the dust sublimation radius (Natta et al. 2000; Tuthill et al. 2001; Dullemond, Dominik & Natta 2001; Muzerolle et al. 2003). In our models, both the central star and the accretion shocks at the stellar surface heat the dusty wall (Muzerolle et al. 2003; D’Alessio et al. 2004). Assuming that the dust population at this radius only consists of silicates with the *small* grain size distribution, using

the silicate sublimation temperature in Table 1, this radius is $R_{sub} = 10 R_*$ for the fiducial parameters. We take this value as the minimum disk radius, since for the range of mass accretion rates and low stellar temperatures considered the gaseous inner disk is probably optically thin, so it does not shadow the wall from stellar radiation and, compared to the irradiated wall, does not contribute appreciably to the SED (Muzerolle et al. 2004).

For consistency, we generally assume that the dust in the wall is settled in the same proportion as the rest of the disk. This assumption affects the estimated height of the wall, which is calculated as the height where the optical depth to the stellar radiation is unity (Dullemond et al. 2001; Muzerolle et al. 2004). Thus, the emergent flux of a wall corresponding to a disk with $\epsilon < 1$ is smaller (because the wall observed area is smaller) than in the $\epsilon = 1$ case.

The treatment described in papers I, II and III corresponds to a disk in which the scattering of stellar radiation is *isotropic*. However, depending on their composition and size, dust grains tend to scatter light in a more forward direction. The extreme case of perfectly forward scattering should give a structure and SED indistinguishable from a case where only true absorption is being considered (Natta et al. 2000). This is the case where the intensity emerging from the upper optically thin layer would be maximum, since the stellar radiation can penetrate and heat the deepest. So, in addition to our calculations with isotropic scattering, we present results for the limiting case of completely forward scattering (i.e., no scattering) to quantify the consequences of these effects.

3. Results

3.1. Effects of dust depletion on the disk structure

In this section we describe the effect of dust settling toward the midplane characterized as described in §2.2 on the disk structure. We compare the results for disk models with settling with those for the well mixed disk model with $a_{max} = 1$ mm that approximately fits the median SED of Classical T Tauri Stars in Taurus (paper III). Table 2 lists different properties of the models discussed here.

The direct consequence of decreasing ζ_{small} is to decrease the opacity to the stellar radiation and thus lower the height of the irradiation surface $z_s(R)$. Figure 3 shows how $z_s(R)$ and $\mu_0(R)$ (cf. §2.1) decrease when ζ_{small} and ϵ decrease. The change in ζ_{small} (or μ_0) affects the irradiation flux, since the smaller the μ_0 the smaller the stellar flux intercepted by the disk and the colder the disk. We see that the well mixed model with $a_{max} = 1$ mm has a μ_0 between the models with $\epsilon = 0.1$ and $\epsilon = 0.01$. The irradiation surface is slightly higher

in the case of ISM dust, because of the higher opacity of this mixture at the wavelength range where the stellar radiation is mostly absorbed (see Figure 2).

For the fiducial models shown in Figure 3, the curvature of the disk surface is not important for $R < 0.2$ AU, and $\mu_0(R)$ is similar to that of a flat disk, $\mu_0 \approx 2/3\pi(R/R_*)^{-1}$. However, at larger radii $\mu_0(R)$ increases with radius, and even for $\epsilon = 0.001$ (i.e., with 0.1 % of the standard dust to gas mass ratio in the absorption layers) $\mu_0(R)$ is larger than for a perfectly flat disk. As Dullemond & Dominik (2004b), we also find that for very low values of ϵ (i.e., a more advanced stage of settling), z_s/R has a maximum (at ~ 100 AU) and decreases for larger radii. This type of geometry led Dullemond & Dominik to argue that the outer disk of highly settled models is in the shadow of inner regions and does not receive stellar radiation. However, the scattering of stellar radiation by dust above z_s and the radial transport of energy would tend to increase the heating of the outer disk and remove the shadowing effect. Since our model is 1+1D we cannot include the scattering in the uppermost layers and the radial transport of energy. In any case, the contribution of disk regions beyond 100 AU to the SED for highly settled models is negligible in the mid-IR, which is the spectral region where the effects of settling are most important (cf. §3.3.)

Figure 4 shows different characteristic temperatures of the disk as a function of radius. The upper panels show the surface temperature T_0 for different values of dust depletion in the upper layers ϵ and the two adopted dust compositions. To show the difference between models in an expanded format we have plotted $\log(T_0 \times R^{1/2})$, because the temperature distribution tends to approximately $T_0 \propto R^{1/2}$ at large radii. One can see that all the models with small grains in the upper atmosphere and the same dust composition have similar $T_0(R)$, regardless the value of ϵ ; this temperature is similar to that of the well mixed model with small grains. This is consistent with what one expects from radiative equilibrium of optically thin dust, in which the heating and the cooling are both proportional to the dust to gas mass ratio, and then the dependence in ζ_{small} (or ϵ) cancels out (§2.1). The small differences are due to the inclusion of the heating of the upper dust grains by radiation emerging from the disk own photosphere (see Calvet et al. 1991).

The cases with P94 dust show discontinuities which are related to the sublimation temperatures of the different ingredients (see Table 1). Comparing temperatures for the ISM and P94 mixtures, one can see that the presence of water ice in the outer disk increases the cooling. For instance, at 100 AU the surface temperature for the models with P94 dust (with water ice) is a factor of 1.4 lower than the surface temperature of the models with ISM dust (without water ice).

The surface temperature of the settled models in Fig. 4 is higher than that of the well mixed model with big grains ($a_{max} = 1$ mm), because small grains are much more efficient

absorbing stellar radiation. However, even for $a_{max} = 1$ mm, $T_0 \times R^{1/2}$ is not constant as expected if grains were blackbodies (i.e., with gray opacities); since we have a grain size distribution such that there is always a fraction of small grains (with $a < \lambda/2\pi$) regardless how big a_{max} is, so that the resulting opacity is not completely gray.

The mid panels of Figure 4 show the midplane temperature as a function of radius. Again, to emphasize the differences between models we plotted $\log(T_c \times R^{1/2})$ in the vertical axis, instead of $\log T_c$. In contrast to the surface temperature, the midplane temperatures show a strong dependence on ϵ , decreasing as ϵ decrease and less stellar energy is captured. The cases with $\epsilon = 0.01$ and 0.001 , have lower temperatures than a well mixed model with $a_{max} = 1$ mm for $R > 10$ AU, as a consequence of the lower irradiation surface of these settled models (Fig. 3).

To see in more detail the dependence of the temperature on ϵ , Figure 5 shows the vertical distribution of temperature at three representative radii: 1, 10 and 100 AU, for both dust compositions and different depletion factors. For comparison we also show the vertical temperature distribution for the well mixed model with $a_{max} = 1$ mm. The behavior of $T(z)$ for well mixed models has been discussed before (Calvet et al. 1991, 1992; Paper II). In short, the temperature has a plateau at $\sim T_0$ at large heights above the midplane, which roughly corresponds to the absorption layer discussed in §2.1. Then, at a height of $\sim 1.3 - 1.4 z_s$ (z_s is indicated in the Figure), the temperature begins to decrease as z decreases, since less stellar energy reaches those layers. Near the midplane at radii in where the disk is thick to its own radiation (cf. $R = 1$ AU in Figure 5), the temperature gradient becomes positive, so that the viscous flux generated near the midplane is transported outward. When the disk becomes optically thin to its own radiation at larger radii (cf. $R = 10$ AU, 100 AU in Figure 5), the midplane becomes nearly isothermal.

As shown in Figure 5, as ϵ decreases and the upper layers become more depleted of grains, stellar radiation penetrates deeper into the disk changing the vertical temperature structure. The upper plateau at T_0 is still present, but it extends deeper into the disk as the height z_s decreases with ϵ . In the dense midplane of the inner regions, temperatures drop because the Rosseland mean optical depth decreases. In the outer regions, as the bulk of the disk becomes more and more optically thin, an increasing amount of stellar radiation, reprocessed by the absorption layers, reaches regions closer to the midplane. $T(z)$ has a further drop in the big grains layer near the midplane; as ϵ decreases, more mass concentrates in this layer, the optical depth of this layer increases, and less energy reaches the level $z = 0$, lowering T_c (cf. Figure 4).

The models presented here are α steady accretion disk models, for which the mass surface density is consistently obtained in terms of the mass accretion rate \dot{M} and the viscosity, which

in the α prescription depends on temperature. Since the temperature structure depends on ϵ , so does the surface density and the disk mass, for the same mass accretion rate. Figure 6 shows $\Sigma \times R$ for models with different depletions (again, to compare with the standard assumption $\Sigma \propto 1/R$). The well mixed model with $a_{max} = 1$ mm is also shown for comparison.

To understand the behavior of Σ , note that with the adopted assumptions, conservation of angular momentum flux gives $\int_0^\infty \rho \nu_t dz = \dot{M}/3\pi(1 - (R_*/R)^{1/2})$, where the viscosity is $\nu_t(z) = c_s/H = \alpha c_s^2(z)/\Omega_k$, with $H = c_s(z)/\Omega_K$, where $c_s(z)$ is the sound speed at z , and Ω_K is the Keplerian angular velocity. This expression is usually approximated in well mixed models as $\Sigma \sim \dot{M}\Omega_k/3\pi\alpha c_s^2(T_m)(1 - (R_*/R)^{1/2})$ with $T_m \sim T_c$, because T_c characterizes the region near the midplane where most of the mass is. However, because we have adopted a z_{big} considerably less than H , most of the disk mass (which is contained within H) is *not* characterized by T_c . In this cases, $T_m = \langle T \rangle$, where $\langle T \rangle$ is the average temperature weighted by the local volumetric mass density; this temperature is shown in the lower panels of Figure 4. The surface density follows the inverse of the average temperature.

At small radii, temperatures within one scale height of the midplane decrease with ϵ (see Fig. 5), so the average temperature decreases and Σ increases. At large radii, the temperature is low at the midplane, but begins to increase in less than one scale height, so that $\langle T \rangle$ increases with ϵ and Σ decreases.

The dependence of Σ on radius can be seen in Figure 6. For $\epsilon = 1$, approximately $\Sigma \propto R^{-1}$ at radii from a few to ~ 200 AU. As ϵ decreases Σ decreases more steeply, with $\Sigma \propto R^{-1.2}$ for $\epsilon = 0.001$. In all cases, $\Sigma \propto R^{-1.4}$ at large radii where the disk becomes optically thin. The corresponding disk masses, calculated from the integration of the surface density, are given in Table 2 for disk radii of 100 AU and 300 AU. For the same mass accretion rate, disks with no depletion are ~ 2 more massive than those with $\epsilon = 0.001$ (0.1 % depletion), because of the lower surface density of the latter. The specific angular momentum of the disk is given by

$$\frac{J_d}{M_d} = 4\pi \int_{R_{mag}}^{R_d} R^3 \Sigma(R) \Omega_K(R) dR / M_d \quad (4)$$

where Ω_K is the Keplerian angular velocity. Using as a reference the angular momentum of an annulus with the disk mass concentrated at the outermost radius, i.e., $(J_d/M_d)^0 = (GM_* R_d)^{1/2} = 3.15 \times 10^{20} (R_d/100AU)^{1/2} cm^2 s^{-1}$, we find that all the models displayed in Table 2 have $J_d/M_d \sim 0.6 - 0.7 (J_d/M_d)^0$.

Given the changes in the temperature and surface density relative to the typical well mixed models with the same mass accretion rate, it is important to quantify the Toomre

parameter of these models to check their stability against self-gravity perturbations. The lower panels of Figure 6 show the Toomre parameter evaluated at the disk midplane,

$$Q \equiv \frac{c_s(T_c)\Omega}{\pi G \Sigma}. \quad (5)$$

We can see that the stability condition $Q \gtrsim 1$ (e.g., Gammie & Johnson 2004) is satisfied at every radius for the present set of parameters.

3.2. Spectral Energy Distributions

Figure 7 shows the SEDs for models calculated with the fiducial parameters and with the two assumed dust compositions. Models are calculated for four values of the depletion parameter ϵ and the two limiting cases of isotropic and completely forward scattering of stellar radiation (§2.2). The SED of the central star was taken from Bruzual & Charlot (1993).

For both dust mixtures and assumptions of scattering properties, the SEDs show a similar general behavior, also described in Dullemond and Dominik (2004). As ϵ decreases, the emission at infrared wavelengths decreases, and the infrared SED becomes steeper. As discussed, this is a consequence of how the irradiation surface changes when the atmospheric dust is depleted (see Figure 3). A lower z_s implies a lower irradiation flux entering the disk and thus a lower emergent flux. However, even for the case of the highest depletion we are considering, the spectral index in the 25 μm - 100 μm region is flatter than that of a perfectly flat disk, $n \sim -4/3 = -1.33$ (see Fig. 7). In other words, the disk is flared even for a dust to gas mass ratio of only 0.1 % the standard value, The slope of the SED in the mid-IR and far-IR depends on the dust composition in addition to ϵ . For instance, the water ice in the P94 mixture produces in emission bands at $\sim 50 - 60 \mu\text{m}$ (cf. Fig. 2), which tend to flatten the SED in this wavelength region relative to the disks with ISM dust.

Figure 7 also shows that the mm flux first increases between $\epsilon = 1$ and 0.1, and then decreases with ϵ . Since the opacity at mm wavelengths is low, the largest contribution to the flux in the mm comes from the dense dust layer near the midplane. Although the dust to gas mass ratio of the big grains layer increases when ϵ decreases (Table 3), the lower temperature at the midplane (Figure 4) results in lower mm fluxes. The mm slope of the SED becomes flatter because the temperature drops to low enough values that the Planck function does not have precisely the Rayleigh-Jeans slope.

Even models with very flat SEDs show emission in the 10 μm silicate feature (Figure 7).

Table 2. Model properties

$\epsilon = \zeta_{small}/\zeta_{std}$	Dust	w	$M_d(100 AU)/M_\odot$	$M_d(300 AU)/M_\odot$	$z_{wall}(R_*)$
1	ISM	$\neq 0$	1.2×10^{-2}	3.2×10^{-2}	1.41
0.1	"	$\neq 0$	1.1×10^{-2}	2.0×10^{-2}	1.23
0.01	"	$\neq 0$	7.8×10^{-3}	1.5×10^{-2}	1.0
0.001	"	$\neq 0$	7.1×10^{-3}	1.4×10^{-2}	0.76
1	ISM	0	1.1×10^{-2}	3.2×10^{-2}	1.12
0.1	"	0	1.1×10^{-2}	2.2×10^{-2}	0.95
0.01	"	0	8.9×10^{-3}	1.6×10^{-2}	0.75
0.001	"	0	7.3×10^{-3}	1.5×10^{-2}	0.47
1	P94	$\neq 0$	1.4×10^{-2}	3.5×10^{-2}	1.41
0.1	"	$\neq 0$	1.3×10^{-2}	2.4×10^{-2}	1.23
0.01	"	$\neq 0$	9.9×10^{-3}	2.0×10^{-2}	1.0
0.001	"	$\neq 0$	9.7×10^{-3}	2.0×10^{-2}	0.76
1	P94	0	1.1×10^{-2}	3.3×10^{-2}	1.12
0.1	"	0	1.3×10^{-2}	2.7×10^{-2}	0.95
0.01	"	0	1.1×10^{-2}	2.2×10^{-2}	0.75
0.001	"	0	9.7×10^{-3}	2.0×10^{-2}	0.47

Notes: w is the albedo. M_d is the disk mass up to the radius inside the parenthesis.

The ratio between the flux at the center of the feature and to the interpolated continuum flux depends on the type of silicate, the assumed dust composition, the asymmetry factor of the grains, and the degree of settling, in addition to the inclination to the line of sight. ISM dust produces a stronger band than P94 dust if scattering is isotropic. The main reason is that the upper atmosphere of the disk with ISM dust is hotter than the case with P94 dust (see Figures 4 and 5). On the other hand, P94 dust has a higher albedo than ISM dust, so the silicate feature flux increases more for P94 than for ISM dust as scattering becomes less isotropic.

In Figure 8 we show the SEDs of Figure 7 with ISM dust in the 1 - 40 μm region, indicating the the separate contributions of the wall at the dust sublimation radius, the disk truncated at this radius, and the stellar photosphere. The wall is a major contributor to the flux shortward of $\sim 10\mu\text{m}$. At the inclination of the fiducial model ($\mu = 0.65$, $i = 50^\circ$) and for this type of dust, the contributions of the wall and the disk are similar at $\lambda \sim 6 - 8\mu\text{m}$, and the wall dominates the excess above the photosphere at shorter wavelengths. The wall contributes $\sim 20\%$ of the flux at 10 μm . As ϵ decreases, the excess above the photosphere decreases.

3.3. Spatial distribution of the emergent flux

Figure 9 shows relative cumulative flux at radius R as a function of radius at representative wavelengths for the fiducial model with ISM dust and two degrees of settling, $\epsilon = 1$ and $\epsilon = 0.001$, and pole-on disks ($\cos i = 1$.) In general, outer regions contribute more flux at longer wavelengths, but the actual contribution of a given region to the flux at a given wavelength depends on ϵ . For both values of ϵ , the short wavelength side of the 10 μm band, emerges from $R < 0.2$ AU, but for longer wavelengths the contribution of regions outside 10 AU becomes less important as ϵ decreases. For $\epsilon = 0.001$, a fraction $\geq 80\%$ of the flux up to 100 μm arises from $R \leq 10$ AU, and $\sim 50\%$ of the millimeter flux is formed inside 30 AU.

In addition to continuum points, Figure 9 shows the region of formation of the 10 μm flux, due to silicate emission. Again, the extent of this region depends on ϵ . For $\epsilon = 1$, 70% of the flux at 10 μm at forms inside 1 AU, while for $\epsilon = 0.001$, 85% forms in this region; in both cases all the flux at 10 μm arises at $R < 10$ AU.

The observed flux at 10 μm will be a sum of emission from the disk and the wall at the dust destruction radius. For $\cos i = 1$ there is no wall contribution because it is assumed to be vertical, but for $i = 50^\circ$, the wall contribution is $\sim 20\%$ (§3.2), and it becomes larger as

inclination increases (until the wall begins to self-shadow, $i \sim 70 - 80^\circ$).

3.4. Radial dependence of ϵ

In this section we study the effect of changing the depletion of the upper layers with radius. To restrict the parameter space, we adopt the following functional form,

$$\epsilon(R) = \begin{cases} \epsilon_1 & \text{if } R < R_1, \\ \epsilon_1(R/R_1)^f & \text{if } R_1 < R < R_2, \\ \epsilon_2 & \text{if } R > R_2 \end{cases} \quad (6)$$

where the exponent of the power law is $f = [\log(\epsilon_2) - \log(\epsilon_1)]/[\log(R_2) - \log(R_1)]$. We adopt $R_1 < R_2$ and $\epsilon_1 < \epsilon_2$, because we assume that dust settling in the inner disk is faster than in the outer disk, since the timescale for settling in a quiescent disk is comparable to the orbital timescale (Weidenschilling et al. 1997; Dullemond & Dominik 2004). Different combinations of the four parameters ϵ_1 , ϵ_2 , R_1 and R_2 produce different SEDs and Figure 10 shows some examples.

In Figure 10, we keep ϵ_1 and ϵ_2 fixed at 0.01 and 0.1, respectively, and show the effect of changing the extent in the disk of the regions with different settling. For comparison, we show models with the corresponding constant values of ϵ . In the left hand side, the inner most settled region extends to 10 AU, and the degree of settling increases to radii 50, 75, and 90 AU. It can be seen that the fluxes up to $\sim 15 \mu\text{m}$ correspond to those of the model with $\epsilon = 0.001$, while for $\lambda > 25 \mu\text{m}$, the fluxes correspond to those of the model with $\epsilon = 0.1$. This is in agreement with the fact that for the large values of ϵ of the outer regions, most of the flux at $\lambda > 25 \mu\text{m}$ comes from regions around 100 AU (see Fig. 9). In the right hand side, the more settled inner disk regions extend to 50 AU, while the transition region extends to 75, 100, and 200 AU. In this case, there is a larger effect on the far-IR fluxes, because the outer disk regions where most of this flux is produced are affected.

3.5. Effect of the grain size distribution in the upper layers

So far, we have shown models in which the upper layers have a fixed maximum grain size of $a_{max} = 0.25 \mu\text{m}$. This value was chosen because it is characteristic for the diffuse ISM (e.g., DL). However, grains might have grown in the cores where disks are formed (e.g. Weidenschilling & Ruzmaikina 1994) and/or small grains might have been blown away from the disk upper layers by radiation pressure. On the other hand, grains with radius

$a = 0.25\mu m$ and smaller might have already settled, leaving only the smallest grains at the upper layers. Figure 11 shows the effect on the SED of values of $a_{max} = 0.05, 1, \text{ and } 10 \mu m$ in the upper layers, for $\epsilon = 0.1$ and 0.001 . We can see that the smaller the grains the stronger the bands, because the grains in the upper atmosphere are hotter when a_{max} decreases. The $10 \mu m$ silicate band almost disappears for $a_{max} > 1 \mu m$. Also, for a given ϵ , smaller grains result in higher IR continuum, reflecting the fact that the small grains absorb the stellar radiation much more efficiently.

3.6. Effect of the height of the layer with large grains

We have assumed so far that the layer of big grains is geometrically thin. This situation might be expected if the disk is old and quiescent enough, such that settling has taken place in the whole disk vertical structure fairly homogeneously. However, during the first stages of settling, only grains from the regions with the lowest density may have settled. Also, as shown by Miyake & Nakagawa (1995), and more recently by Dullemond & Dominik (2004), the turbulence described by an α prescription may be able to mix grains up to several scale heights.

In this section we explore the effect in the SED of adopting different heights for the big grains layer, z_{big} (see Figure 1). We parameterize the height of the big grains layer as a constant times the local gas scale height $H = c_s(T)/\Omega_k$. The assumption that the layer of big grains at the disk midplane is geometrically thin is relaxed, and we calculate ζ_{big} for each z_{big} consistently for each value of ϵ (see Appendix). As described in papers I, II and III, the calculation of the disk structure is performed using an iterative scheme in order to obtain the irradiation surface and the disk structure self-consistently. In the case of z_{big}/H of order 1 or larger we numerically integrate the density over the different disk regions in each one of these iterative steps.

Figure 12 shows SEDs for the fiducial model with ISM dust, isotropic scattering, $\epsilon = 0.1$ and 0.01 , and different values of z_{big} . The upper left panel shows the cases with $z_{big} = 0.1H$, for comparison. As shown in the upper right panel, SEDs for $z_{big} \leq 1H$ are very similar to the thin layer case, because the irradiation surface is still well above z_{big} , and its location depends on the small grains and their depletion; in these cases, the optically thin emission from the upper hot atmosphere is dominated by the emissivity of the small grains. However, as z_{big} increases and ϵ decreases, the irradiation surface moves closer to the region with large grains. The near-IR SED of cases with $z_{big} = 2H$ corresponds to that of an atmosphere with small grains, because at small radii the irradiation surface is still above z_{big} ; however, the far IR SEDs tends toward the SED of the well mixed disk with $a_{max} = 1 \text{ mm}$, becoming more

similar as ϵ decreases. In the extreme case of $z_{big} = 3H$, the two models with different values of ϵ have the same SED than the well mixed model with $a_{max} = 1$ mm and no depletion. In this case the dust mass of the layers above z_{big} is negligible compared to the dust mass below, and the dust to gas mass ratio of the big grains layer is close the standard value.

3.7. Dependence on mass accretion rate

Our models are for *accretion disks* irradiated by the central star. The fact that these are accretion disks enters in three ways into our model calculations. First, viscous dissipation is considered an additional disk heating source. This heating mechanism is important close to the star and close to the midplane, to an extent dependent upon the ratio of L_{acc} to L_* . In those regions where viscous dissipation significantly alters the midplane temperature, the gas scale height also changes, affecting the whole vertical density distribution and, consequently, the height of the irradiation surface and the reprocessed stellar flux. In addition, the energy flux released by viscous dissipation modifies the SED with respect to a purely reprocessing disk. Second, the inner edge of the dusty disk is irradiated both by the star and by the accretion shocks at the stellar surface, where disk material is channeled onto the star by the stellar magnetosphere (Muzerolle et al. 2003; D’Alessio et al. 2003). Third, the disk density depends on the mass accretion rate through the conservation of angular momentum flux. The disk mass surface density is proportional to \dot{M}/ν_t , where ν_t is a density weighted mean turbulent viscosity coefficient (c.f., §3.1). Thus, the higher the mass accretion rate, the higher the disk density, and the higher the irradiation surface. As a consequence, disks with higher mass accretion rates will have higher fluxes, even if turbulent viscous dissipation is not as important as stellar irradiation as the disk heating mechanism. Correspondingly, disks of the same outer radius and the same α with higher accretion rates will have larger masses.

Figure 13 shows the effect on the SED of changing the mass accretion rate and the degree of settling. It clearly can be seen that the mid and far IR and sub-mm and mm fluxes scale with \dot{M} for a given value of ϵ . It can also be seen that even the case with the largest mass accretion rate shown, the emergent SED depends on ϵ , because irradiation is still an important heating mechanism. As previously shown by Calvet et al. (1991), the intensity of the 10 μ m silicate band decreases as mass accretion rate increases, because of the decrease in the contrast between the temperatures at the silicate band formation height and the continuum formation height. However, the present models do not include the disk irradiation by the accretion shocks at the stellar surface, which might be an important irradiation source for $\dot{M} \gtrsim 10^{-7} M_\odot \text{yr}^{-1}$ (D’Alessio et al. 2004) and which probably would

increase the gradient of temperature in the disk atmosphere. The role of this irradiation source will be discussed in a forthcoming paper.

3.8. Dependence on inclination angle

Figure 14 shows the SEDs of the fiducial model with ISM dust for 4 different high inclination angles: $\cos i = 0.1, 0.25, 0.35$ and 0.5 (i.e., $i = 84, 75.5, 69.5$ and 60°), and different degrees of settling: $\epsilon = 1, 0.1, 0.01$ and 0.001 . All the SEDs include the contribution of the star and the wall, the thermal emission from the disk, and the contribution of the stellar light scattered in the disk atmosphere and the disk thermal emission.

At high inclinations, the flared outer disk regions absorb radiation from the star, wall, and inner disk. For a given inclination, disk surface density distribution and outer radius the resultant extinction depends on ϵ ; as the disk becomes more settled and geometrically flatter, the range of inclination angles for which the outer disk occults the star is narrower.

In the models with the highest inclination angle in the upper right corner of Figure 14, $\cos i = 0.1$, the star contributes only indirectly to the SED through scattered light in the case $\epsilon = 1$. This produces a characteristic double-bump shape. Notice that the thermal emission of an highly inclined disk might be similar to that of a class I/0 source (Chiang & Goldreich 1999) but the contribution of the scattered light makes the total SED very different to a class I/0 source and even to a class II source (see paper II). As ϵ decreases and the outer disk becomes flatter, the peak of the thermal emission moves toward shorter wavelengths and the silicate absorption feature becomes shallower, reflecting the decreased opacity of the outer regions. At the same time, the lower the ϵ , the lower the far-IR flux of the disk as it intercepts less radiation from the star. All these edge-on models have similar contributions of scattered stellar light, since it depends on the albedo which is independent on dust to gas mass ratio.

The rest of the panels in Figure 14 show the SEDs for lower inclinations. Occultation effects including silicate absorption are still present, but they only affect the less settled objects as inclination decreases. Mid- and far-IR continuum fluxes increases roughly proportional to $\cos i$, as expected for an optically thick, geometrically flat disk, while the optically thin millimeter fluxes are independent of inclination.

4. Observational tests

4.1. Median SED of CTTS in Taurus

Figure 15 compares the predictions of our fiducial settled models with median fluxes for the Taurus population. For $\lambda < 10\mu\text{m}$, the median values and quartiles were constructed from the 2MASS and IRAC magnitudes of Hartmann et al. (2005). This sample consists of 19 stars. Fluxes were scaled to the H band, after correcting for reddening as in Furlan et al. (2005b). At longer wavelengths, we show the median from Paper II. We also show in Figure 15 predictions for the fiducial model with ISM dust and two values of $\epsilon = 0.1$ and 0.01 . The models are shown for two inclinations, 30° and 60° ($\mu = 0.87$ and 0.5), because as already mentioned, the median may correspond to inclinations lower than $\mu = 0.5$ if the highly inclined objects are too extinguished to be included in the sample. The models have been corrected for self-extinction, to make a consistent comparison with a sample corrected for reddening.

For $\lambda < 6\mu\text{m}$, model predictions are roughly consistent with the IRAC median. The models are slightly below the median values at the IRAC bands, even though we have assumed no settling in the inner wall to increase the wall emission and thus short-wavelength fluxes. Several factors may play a role in accounting for these differences. First, photospheric fluxes have a large contribution at these wavelengths, and details of the adopted SEDs can affect the comparison. Here we have added the excess disk + wall fluxes to the dereddened fluxes of the Weak (non-accreting) T Tauri star HBC 274 from Hartmann et al. (2005), which may be more representative of the active photospheres of the stars. Second, if true accretion rates are higher than the assumed $\dot{M} = 10^{-8}M_\odot\text{yr}^{-1}$, the near-infrared fluxes would increase. As can be seen in Figure 13, the near-IR flux increases more rapidly for $\dot{M} > 10^{-8}M_\odot\text{yr}^{-1}$ than it decreases for $\dot{M} < 10^{-8}M_\odot\text{yr}^{-1}$. This is due to the fact that for $\dot{M} < 10^{-8}M_\odot\text{yr}^{-1}$, the radius of the wall is effectively set by the stellar luminosity, while for larger rates, the wall radius increases as the accretion luminosity increases and becomes more comparable to the stellar luminosity. The uncertainty in the mass accretion rate determinations is probably a factor 2 or even perhaps 3; increasing the mean accretion rate would improve the agreement with the median SED. Third, the geometry of the wall may play a role. We have assumed that the wall is vertical for simplicity, but the actual geometry may be more rounded because of the height dependence of the density (Isella & Natta 2005). If this is the case, the more area of the wall may be exposed and the inclination dependence we have used is no longer valid. A more detailed study of the inner disk regions, including information from interferometric measurements (Akeson et al. 2005; Eisner et al. 2005), may clarify these points further.

Although the models appear to be low at $8\mu\text{m}$, this cannot be trusted, because the IRAC band is not a monochromatic measurement but instead includes some silicate emission in its bandpass. Detailed comparisons require the data forthcoming from the Infrared Spectrograph on the Spitzer Space Telescope. In a separate paper (D’Alessio et al. 2005c, in preparation) we carry out a detailed exploration of the effects of different compositions of the dust, in particular of the silicates, and show that the silicate feature can be reproduced in individual cases assuming a large variety of compositions, in agreement with detailed determinations by B. Sargent et al. (2005, in preparation).

The models reproduce in general terms the long wavelength median SED, as already pointed out by Furlan et al. (2005a). While it appears that the mid-IR is better reproduced by models with $\epsilon = 0.1$ with smaller values of ϵ are required at longer wavelengths, it should again be noted that the median SED in this region is derived from IRAS observations, and the comparisons will need to be revisited once detailed *Spitzer* results become available.

In addition, the model fluxes in the millimeter range are slightly lower than the median fluxes. This may be remedied by models where the layer with big grains covers a larger height in the disk. to illustrate this, we show in Figure 15 a model with $\epsilon = 0.1$ and $z_{big} = 2$ H from Figure 12, which seems to improve the comparison. In any event, more information about degrees of settling in real objects require detailed modeling of individual SEDs.

4.2. IRAC colors of Taurus CTTS

Figure 16 shows IRAC colors of CTTS in Taurus from Hartmann et al. (2005). The central wavelengths of these bands are $3.6\mu\text{m}$, $4.5\mu\text{m}$, $5.8\mu\text{m}$, and $8\mu\text{m}$, covering the wavelength region shortwards of the silicate feature with an important or dominant contribution from the wall at the dust destruction radius (except at extremely low or high inclinations to the line of sight). As discussed, this wavelength region is actually probing the innermost disk (Figure 9). Model colors have been constructed by adding excess emission fluxes (disk + wall) integrated over the band transmissions to those of the Weak T Tauri star HBC 274 from Hartmann et al. (2005), of spectral type K7 scaling to the same luminosity as the model, to make sure that the colors tend to observed photospheric colors when the excess tends to zero.

Models are shown for several values of mass accretion rate, settling parameter, and inclination (see caption to Figure 16). For a given value of ϵ , predicted colors increase with mass accretion rate, as the emission from the disk and specially the wall at the dust destruction radius increases (§3.2, §3.7, and Figure 13).

The largest inclination dependence of colors is seen for models with high mass accretion rate and/or large values of ϵ . This is due to the effects of disk self-absorption in these optically thicker models (§3.8 and Fig. 14). In particular, models at the higher inclination shown in Figure 16 ($\cos i = 0.25$) tend to have very *red* [3.6]-[4.5] color and very *blue* [5.8]-[8] color; the SED of the $\epsilon = 1$ model in upper right panel of Fig. 14 has these colors: a very red slope shortwards of the silicate feature, and a deep silicate absorption, which results in a low flux in the broad IRAC [8], and in a blue [5.8]-[8] color.

Colors [3.6]-[4.5] and [4.5]-5.8] become bluer as the settling parameter decreases, reflecting the decrease of flux of the the inner disk. The reddest values of the [5.8]-[8] color are not predicted by the models. Since the [8] band has a large contribution from the silicate emission feature, this is the same problem encountered when discussing the median SED (§4.1).

Overall, the observed range of IRAC colors in Taurus can be explained by the predictions of settled models; settling has only modest effects on the colors in this wavelength range. Slightly better agreement is obtained at somewhat higher mass accretion rates than the fiducial $\dot{M} = 10^{-8} M_{\odot} \text{yr}^{-1}$. It is difficult to compare our results with those of Whitney et al. (2003, 2004) because they exhibit very few disk models for low-mass stars.

4.3. Mid-IR spectral slopes

Furlan et al. (2005a) calculated slopes of the fluxes in *Spitzer* Infrared Spectrograph (IRS) spectra of a sample of CTTS in Taurus, using continuum bands (i.e., free from features) of spectra from Spitzer IRS. The center wavelength of the selected bands are 5.7, 7.1, 13.25, 16.25 and 25 μm . Figure 17 shows the logarithm of the ratio of fluxes 13/25 and 6/25 (rounding up with central wavelengths of the bands to the nearest digit), denoted by indices, from Furlan et al. (2005a) compared to predictions for the fiducial model with ISM dust with different mass accretion rates, inclination angles, and values of ϵ .

Except for models with $\epsilon = 1$, the value of the indices increases with inclination. This is due to the fact that as inclination increases the wall emission increases (up to $\sim 70^\circ$), increasing the 6 μm flux and to a lesser extend the 13 μm flux, while disk emission at 25 μm decreases (Fig. 14). For models with $\epsilon \sim 1$, the short wavelengths are self-absorbed and the indices decrease.

Most of the observations fall in the region corresponding to mass accretion rates $10^{-9} M_{\odot} \text{yr}^{-1}$ and $10^{-8} M_{\odot} \text{yr}^{-1}$, and inclinations 30° and 60° , as expected. Moreover, as already discussed in Furlan et al. (2005a) the observations are consistent with values of settling $\epsilon \leq 0.1$.

4.4. Scattered light images of edge-on disks

In Paper III we showed that disk models with larger grains have less opacity to the stellar radiation producing flatter images in scattered stellar light when disks are seen edge-on. The flattening of the near-IR images of edge-on disks with respect to what is predicted if disks have ISM-like dust (c.f., paper II) was required to explain cases like HH 30 and HK Tau B.

As expected, a similar flattening of the image results from increasing the depletion of small grains in the upper layers. Figure 18 shows how the distance between the bright nebulae and the width of the dark lane decrease when ϵ decreases, because the upper layers becomes more transparent to stellar radiation. We do not attempt a detailed modeling of any object at this time, but aim to show that the image of an edge-on disk with certain degree of settling is consistent with the image of an edge-on disk with well mixed big grains. It is possible to distinguish between both cases when there is information available at several wavelengths. For instance, combining scattered light images, a complete SED, and detailed modeling, it seems possible to quantify the upper and lower grain sizes and the degree of settling of a given object, if its mass accretion rate and central star properties are known.

5. Discussion

5.1. Dependence on assumptions

Within the context of our assumptions of an initial (protostellar) dust distribution consistent with that of the diffuse ISM, power-law grain size distributions, and no radial dependence of dust properties, we can only explain the combination of high mm-wavelength emission and ubiquitous $10\mu\text{m}$ silicate emission with a combination of both dust growth (to explain the long-wavelength fluxes) and settling (to move large grains to the midplane, leaving behind small grains to produce strong silicate features), as suggested in Paper III. In principle, we could also obtain this result without settling by having the large grains only at large disk radii, so they can dominate the long-wavelength emission but not contribute to the silicate features; however, this seems unlikely given that dust evolution is likely to be fastest in the inner disk.

Quantifying the degree of settling in a disk from observations is much more difficult. Models of dust evolution suggests that the timescale for settling is proportional to the orbital time (Weidenschilling 1997; Dullemond & Dominik 2004); however, these models predict a much rapid evolution of dust sizes and faster settling than consistent with what is observed

in systems of ages of a few Myr. Other factors such as turbulence, grain shape, and a more complete treatment of particle interaction may be required to obtain closer agreement with observations (Dullemond & Dominik 2005). Given all the theoretical uncertainties, the parameterized treatment given here can provide a useful comparison with observations.

In §2.1, we discussed that the degree of depletion in the disk upper layers required to fit the slope of the SED - indicative of large grains - and at the same time have silicate emission - requiring small grains - was set by the condition that the opacity in the wavelength range where the stellar radiation is absorbed, due to the small grains in the upper layers, had a similar value to that of large grains. This condition can be attained either by (1) decreasing the dust to gas mass ratio in the upper layers or (2) decreasing the opacity per small grain at the stellar wavelengths, while keeping the opacity at longer wavelengths similar, because for a given dust to gas mass ratio different combinations of dust ingredients, optical constants, grain sizes and shapes can produce different wavelength dependences of the opacity. Can we distinguish between these two possibilities?

The continuum flux emerging from the disk interior regions, for a given central star, disk inclination angle, and mass accretion rate, depends on the angle between the incoming radiation and the normal to the disk surface, which is determined by the mean opacity to the stellar radiation. In both possibilities above, depletion or decreased opacity per dust mass, the disk would have the same irradiation surface, and thus similar flux from the interior layers. However, the flux emerging from the optically thin upper hot layers would be different. In the case of lower opacity per grain, the temperature of the upper layers T_0 , given by eq.(2) would be lower, since it depends on the ratio $(\kappa_*/\kappa_P)^{1/4}$, and κ_P is nearly constant for $T < 1000K$ (D’Alessio 1996). The emission of these layers, as given by eq.(1) will also decrease although it depends on $1/\chi_*$, because the decrease due to the exponential dependence on temperature in $B_\nu(T_0)$ would dominate. Since the emission from the upper layers constitutes a significant fraction of the total flux in the mid-IR (Chiang & Goldreich 1997), the case with high k_* and depletion has a larger mid-infrared flux than the case of lower opacity per dust mass, essentially because the small dust is hotter. This means that in principle, the two possibilities could be distinguished by matching the overall SED of actual objects.

A further complication is related to the way in which the optically thin dust temperature is calculated. It is now accepted that in the uppermost layers of the disk, where densities are very small, the gas temperatures is higher than the dust temperature (Glassgold et al. 2004). Moreover, different dust ingredients and grains sizes are characterized by different temperatures since each grain is heated mostly by the absorption of the stellar radiation it intercepts, which depends on its specific absorption coefficient (e.g., Li & Greenberg 1998).

However, close to the irradiation surface the disk density is high enough to assure thermal coupling between gas and dust, and that the main heating mechanism is the dust absorption of stellar radiation (Kamp & Dullemond 2004).

5.2. Impact of settling on disk ionization structure

Sano (1999) and Sano et al. (2000) considered the effect of the dust in calculating the ionization state of protoplanetary disks, with the goal of understanding the location and size of the region where the magnetorotational instability can operate. They find that with a interstellar values for the dust to gas mass ratio and the grain sizes, and assuming a standard cosmic ray ionizing flux, the ionization fraction is such that Ohmic dissipation makes the disk stable inside ~ 20 AU. However, they also find that dust growth and depletion decreases the size of this region, allowing turbulence to be generated by the magnetorotational instability in most of the disk. This occurs because the small dust particles are particularly effective in enhancing the recombination of electrons and ions. In all their models there is a remaining *dead zone* (Gammie 1996) close to the star, with a size that depends not only on ϵ and a_{max} but also on the disk mass surface density. The fiducial disk model of Sano et al. (2000) has the minimum solar mass surface density, which has a steeper dependence on radius than in our models, and thus is higher than the α accretion disk mass surface density for $R < 100$ AU (if $\dot{M} = 10^{-8} M_{\odot} \text{yr}^{-1}$ and $\alpha = 0.01$). Sano et al. show that lowering the mass surface density also has the effect of decreasing the size of the dead zone. A rough comparison with Sano et al. results suggests that a model with $\dot{M} = 10^{-8} M_{\odot} \text{yr}^{-1}$, $\alpha = 0.01$ and $\epsilon = 0.01$ would have a dead zone a factor of 0.1 smaller than their fiducial model (i.e, at $R < 2$ AU). A detailed calculation of the ionization state of a settled accretion disk model is required to quantify the limits of the stable region properly.

5.3. Dust settling and shadowed disks

The possibility of disks being self-shadowed has been raised in a series of studies of disks around Herbig Ae/Be stars (Dullemond & Dominik 2004a, and references therein), and more recently in the exploration of dust settling by Dullemond & Dominik (2004b). This last study was the first to point out the main effect of dust settling on the SED of protoplanetary disks, namely, the decrease of mid to far-IR excess with dust settling. One of the inferences of the Dullemond & Dominik (2004b) study is that the outer portions of the very settled disks are self-shadowed; similarly, we find that the disks with the larger degree of settling in our study, $\epsilon < 0.01$, become optically thin to the stellar radiation outside \sim

100 AU (Fig. 3), so that the disk surface is no longer flared in those outer regions. However, one important point to notice is that the decrease of IR fluxes is not due to the fact that those outer regions are shadowed by the inner disk regions. As discussed in §3.3 and shown in Figure 9, as ϵ decreases, an increasing contribution of the flux comes from the innermost regions of the disk, which are optically thick to the stellar radiation and so still have a flared surface.

Shadowing effects are more likely to be present if the surface density decreases more steeply with radius than $\sim R^{-1.5}$, as shown for the case of the Herbig Ae/Be stars by Dullemond & Dominik (2004a). If this is the case, the density in the outer disk becomes low enough to render it optically thin to the stellar radiation. However, in our studies, the surface density distribution is not a free function, but is calculated self-consistently from the mass accretion rate, the α parameter, and the disk temperature distribution. From these calculations, we obtain not only the absolute value of Σ , consistent with the mass accretion rate, but also the dependence on radius. From Fig. 6 we see that $\Sigma \propto R^{-1}$ for most of the disk; even for the most settled disks, $\Sigma \propto R^{-1.2}$, except in the outermost regions, where it falls like $\propto R^{-1.4}$ (§3.1).

Our calculations rely on the assumption of a steady disk, of course, which may not be an appropriate assumption. Nonetheless, detailed analysis of the surface density distribution of the nearby, and thus bright and clearly resolved disk around TW Hya indicates that it is consistent with the predictions of irradiated disks models (Wilner et al. 2000, 2003, 2005; Qi et al. 2004).

6. Summary and Conclusions

We have explored models of irradiated accretion disks where dust settling has taken place, modifying the vertical distribution of grain sizes and abundances. In these models, dust settling is described in a parametric way, using two populations of grains: micron interstellar-like grains in the upper layers, with a reduced dust to gas mass ratio, and mm-sized grains in the lower layers, with an increased dust to gas mass ratio. The degree of settling is parameterized in terms of the depletion of the upper layers ϵ (settling increases when ϵ decreases) (see §2.2).

We have found that settling affects the disk structure and SED in different ways:

1. The height of the irradiation surface decreases with the degree of settling, decreasing the fraction of stellar radiation intercepted by the disk and, consequently, the far IR excess emitted by the disk. The degree of settling affects the degree of flaring of the

disk. However, even a degree of depletion as low as 0.1 % of the standard value, produces a SED with a larger IR excess than a perfectly flat disk, reflecting the fact that a very small amount of small dust grains at a few scale heights is enough to absorb a larger fraction of stellar radiation than predicted by the flat disk approach (§3.2 and Fig. 7).

2. The surface temperature of the disk is independent on the degree of settling but depends on grains sizes and composition. In contrast, the midplane temperature decreases as the degree of settling increases and less stellar radiation is captured by the disk. (Figs. 4 and 5) This affects the millimeter fluxes emitted by the disk.
3. The mass surface density is as expected for a steady α disk, when the viscosity is taken to be a vertical average weighted by mass. The resultant radial dependence of the surface density over most of the disk varies from $\sim R^{-1}$ for no depletion to $\sim R^{-1.2}$ for the most settled models (§2.2 and Fig. 6). $\Sigma \propto R^{-1.4}$ at large radii where the disk becomes optically thin. All the models with $\dot{M} = 10^{-8} M_{\odot} \text{ yr}^{-1}$ are gravitationally stable, with the Toomre parameter higher than ~ 10 .
4. The 10 μm silicate band appears in all the models with $a_{max} < 10 \mu\text{m}$ in the upper layers, even in those with very small values of ϵ (§3.5 and Fig. 11). The band is not affected much by the upper grains dust to gas mass ratio, but the continuum is. The intensity of the band increases if the size of the grains in the upper layer decrease, because they hotter (§3.5 and Fig. 11), and if the scattering of stellar radiation is forward instead of isotropic, because the stellar radiation can then penetrate and heat to deeper layers.
5. The predicted half-size (region where 50% of the flux arises) of the 10 micron emission is smaller than 0.5 AU. For non settled-disks, the predicted 25 micron half-size can be ~ 10 times larger than the predicted 10 micron half-size. However, as the degree of settling increases, the half-size of mid-infrared emission decreases, as the optical depth of the outer disk decreases (§3.3 and Figure 9).
6. Disk models calculated with a degree of settling that changes with radius from ϵ_1 to ϵ_2 , show SEDs intermediate between two cases with constant depletions (§3.4 and Fig. 10).
7. Disk models calculated with increasing heights of the transition zone between both grain populations show SEDs with characteristics of small grains at small radii and big grains at larger radii (§3.6 and Fig. 12).

8. Disk models with different mass accretion rates have mid- and far-IR, sub-mm and mm fluxes that scale with \dot{M} for a given value of ϵ . The higher the \dot{M} , the lower the contrast between the temperatures where the continuum and the $10\ \mu\text{m}$ band forms, and the lower the flux in the band relative to the continuum (§3.7 and Fig. 13).
9. "Edge-on" disk models have no direct contribution of emission from the central star, which is being extinguished by the outer disk, but show the stellar scattered light component which along with the thermal component produces a double bump SED. As ϵ becomes smaller, the disk becomes flatter and the star less extinguished. The $10\ \mu\text{m}$ silicate band appears in absorption for the high inclined disks, except when ϵ is very small (§3.8 and Fig. 14).
10. The median and the observed slopes in the 3 - 30 μm range from IRS spectra of CTTS in Taurus can be interpreted with models with $\epsilon \leq 0.1$. A model where the height of the layer with large grains is ~ 2 scale heights reproduce better the far-IR and millimeter median fluxes of Taurus (Figs. 15, 16, and 17).
11. Comparison with the median IRAC fluxes of Taurus indicates a deficit of flux in the near-IR and $10\ \mu\text{m}$ silicate feature when compared to models with ISM dust (Fig. 15). This suggests that a better treatment of the inner disk region, including more realistic silicate opacities is necessary.
12. The outermost regions of very settled disks are optically thin and probably are in the shadow of the inner disk, as indicated by Dullemond & Dominik (2004). However, for our disks where the surface density distribution is self-consistently calculated, most of the flux of the very settled disks arises in the inner regions, $< 50AU$, even at long wavelengths, so the effects of the shadows would be difficult to detect (§3.3 and Fig. 9).

Overall, we have shown that the main features in observations of T Tauri disks can be explained with models where the upper layers are depleted of dust by a factor of ten or more. We have explored the parameter space covered by CTTS, and have shown the main effects on the SEDs of these assumptions. Our models admittedly have many simplifying assumptions. Interpretation of the actual SEDs of individual stars will provide a better estimate of the extent and degree of grain growth and settling, and thus of the degree of dust evolution. Efforts to model individual objects with detailed SEDs will be attempted in forthcoming papers.

PD acknowledges support from Grants from UNAM and CONACyT. NC and LH acknowledge support from NASA Grants NAG5-9670, NAG5-13210, and NNG05G126G.

7. Appendix

Given a power law grain size distribution, the constant n_0 is

$$\frac{n_0}{n_H} = \frac{3\zeta m_H \mu (4-p)}{4\pi \rho_d (a_{max}^{4-p} - a_{min}^{4-p})}, \quad (7)$$

where n_H is the density of hydrogen nuclei, m_H is the mass of hydrogen, μ is the mean molecular weight relative to hydrogen, and ρ_d is the bulk density of the grain material.

The mass surface density of dust in the big grains layer is

$$\Sigma_{down}^d = 2\zeta_{big} \int_0^{z_{big}} \rho dz \quad (8)$$

where ρ is the volumetric density of gas. On the other hand, the mass surface density of dust that has disappeared from the upper disk regions is

$$\Sigma_{up,lost}^d = 2\zeta_{std} \left[1 - \frac{\zeta_{small}}{\zeta_{std}} \right] \int_{z_{big}}^{\infty} \rho dz \quad (9)$$

where we assume that the original distribution of dust (before settling starts) has a standard dust to gas mass ratio, ζ_{std} . In other words, the total dust mass surface density is $\Sigma_d = \zeta_{std} \Sigma$, where Σ is the mass surface density of gas, i.e., $\Sigma = 2 \int_0^{\infty} \rho dz$.

Assuming that all the mass in dust lost by the upper regions is down, in the big grains layer, then

$$\Sigma_{down}^d = 2\zeta_{std} \int_0^{z_{big}} \rho dz + \Sigma_{up,lost}^d \quad (10)$$

Thus,

$$\frac{\zeta_{big}}{\zeta_{std}} = \left[\int_0^{z_{big}} \rho dz + \left(1 - \frac{\zeta_{small}}{\zeta_{std}} \right) \int_{z_{big}}^{\infty} \rho dz \right] / \int_0^{z_{big}} \rho dz \quad (11)$$

Lets consider z_{big} as a small fraction of the gas scale height, i.e., $z_{big} \approx \delta H$, thus the integrals can be approximated as following

$$\int_0^{\delta H} \rho dz \approx \rho_0 \delta H \approx \frac{\Sigma}{\sqrt{2\pi}} \delta \quad (12)$$

$$\int_{\delta H}^{\infty} \rho dz \approx \frac{\Sigma}{2} - \frac{\Sigma}{\sqrt{2\pi}}\delta \quad (13)$$

Using these approximations (only valid for $\delta \ll 1$),

$$\frac{\zeta_{big}}{\zeta_{std}} = \left[1 + \left(\frac{\sqrt{2\pi}}{2\delta} - 1 \right) \left(1 - \frac{\zeta_{small}}{\zeta_{std}} \right) \right] \quad (14)$$

In table 3 we list ζ_{big}/ζ_{std} for the values of $\zeta_{small}/\zeta_{std}$ we use in this paper.

In order to avoid numerical problems, we make a smooth transition between both dust populations such that,

$$\zeta_{big}(z) = 0.5\zeta_{big,0} \left\{ 1 + \tanh \left[k \left(1 - \frac{z}{\delta H} \right) \right] \right\} \quad (15)$$

$$\zeta_{small}(z) = 0.5\zeta_{small,0} \left\{ 1 - \tanh \left[k \left(1 - \frac{z}{\delta H} \right) \right] \right\} \quad (16)$$

where we have adopted $k = 20$, $\delta = 0.1$, and the values of $\zeta_{big,0}$ and $\zeta_{small,0}$ are those listed in table 3.

The midplane layer of big grains has a dust to gas mass ratio larger than standard, in order to account for the dust that has settled from upper layers.

REFERENCES

- Aikawa, Y., & Herbst, E. 2001, *A&A*, 371, 1107
- Akeson, R. L., et al. 2005, *ApJ*, 622, 440
- Beckwith, S.V.W., Sargent, A.I., Chini, R. S., & Guesten, R. 1990, *AJ*, 99, 1024 (BSCG)
- Beckwith, S.V.W., & Sargent, A.I. 1991 *ApJ*, 381, 250 (BS91)
- Bergin, E., Calvet, N., D’Alessio, P., & Herczeg, G. J. 2003, *ApJ*, 591, L159
- Bruzual A., G., & Charlot, S. 1993, *ApJ*, 405, 538
- Calvet, N., Patiño, A., Magris, G., & D’Alessio, P. 1991, *ApJ*, 380, 617 .
- Calvet, N., Magris, G., Patiño, A., & D’Alessio, P. 1992, *Rev. Mex. Astronom. Astrofís.*, 24,

- Calvet, N., D'Alessio, P., Hartmann, L., Wilner, D., Walsh, A., & Sitko, M. 2002, *ApJ*, 568, 1008
- Chiang, E.I., & Goldreich, P., 1997 *ApJ*, 490, 368 (CG)
- Chiang, E. I., Joungh, M. K., Creech-Eakman, M. J., Qi, C., Kessler, J. E., Blake, G. A., & van Dishoeck, E. F. 2001, *ApJ*, 547, 1077
- Chiang, E. I. and Goldreich, P. 1999, *ApJ*, 519, 279
- Cohen, M. and Witteborn, F. C. 1985, *ApJ*, 294, 345
- Cotera, A. S. et al. 2001, *ApJ*, 556, 958
- D'Alessio, P. 1996, Ph.D. Thesis, Universidad Nacional Autónoma de México, México
- D'Alessio, P., Cantó, J., Calvet, N., & Lizano, S. 1998, *ApJ*, 500, 411 (DCCL) (Paper I)
- D'Alessio, P., Calvet, N., Hartmann, L., Lizano, S. and Cantó, J. 1999, *ApJ*, 527, 893 (Paper II)
- D'Alessio, P., Calvet, N., & Hartmann, L. 2001, *ApJ*, 553, 321, (Paper III)
- D'Alessio, P., Calvet, N., Hartmann, L., Muzerolle, J., & Sitko, M. 2004, *IAU Symposium*, 221, 403
- Draine, B. T., & Lee, H. M. 1984, *ApJ*, 285,89
- Dullemond, C. P., Dominik, C., & Natta, A. 2001, *ApJ*, 560, 957
- Dullemond, C. P., & Dominik, C. 2004a, *A&A*, 417, 159
- Dullemond, C. P., & Dominik, C. 2004b, *A&A*, 421, 1075
- Dullemond, C. P., & Dominik, C. 2005, *A&A*, 434, 971
- Eisner, J. A., Hillenbrand, L. A., White, R. J., Akeson, R. L., & Sargent, A. I. 2005, *ApJ*, 623, 952
- Forrest, W. J., et al. 2004, *ApJS*, 154, 443
- Furlan, E., et al. 2005, *ApJ*, 628, L65
- Gammie, C. F. 1996, *ApJ*, 457, 355

- Gammie, C. F., & Johnson, B. M. 2004, Workshop on Chondrites and the Protoplanetary Disk, 9115
- Glassgold, A. E., Najita, J., & Igea, J. 2004, ApJ, 615, 972
- Hartmann, L. 2003, ApJ, 585, 398
- Hartmann, L., Megeath, S.T., Allen, L., Luhman, K., Calvet, N., D'Alessio, Franco-Hernandez, R., & Fazio, G., ApJ, in press
- Isella, A., & Natta, A. 2005, A&A, 438, 899
- Kamp, I., & Dullemond, C. P. 2004, ApJ, 615, 991
- Kenyon, S.J., & Hartmann, L. 1987, ApJ, 323, 714 (KH87)
- Kenyon, S. J., Hartmann, L. W., Strom, K. M., & Strom, S. E. 1990, AJ, 99, 869
- Kenyon, S.J., & Hartmann, L. 1995, ApJS, 101,117 (KH95)
- Li, A., & Greenberg, J. M. 1998, A&A, 331, 291
- Miyake, K., & Nakagawa, Y. 1993, Icarus, 106, 20 (MN93)
- Miyake, K., & Nakagawa, Y. 1995, ApJ, 441, 361
- Muzerolle, J., Calvet, N., Hartmann, L., & D'Alessio, P. 2003, ApJ, 597, L149
- Muzerolle, J., D'Alessio, P., Calvet, N., & Hartmann, L. 2004, ApJ, 617, 406
- Natta, A., Meyer, M.R., Beckwith, S.V.W. 2000, ApJ,534, 838
- Pollack, J. B., Hollenbach, D., Beckwith, S., Simonelli, D. P., Roush, T. & Fong, W. 1994, ApJ, 421, 615 (P94)
- Qi, C., et al. 2004, ApJ, 616, L11
- Sano, T. 1999, Star Formation 1999, Proceedings of Star Formation 1999, held in Nagoya, Japan, June 21 - 25, 1999, Editor: T. Nakamoto, Nobeyama Radio Observatory, p. 247-248, 247
- Sano, T., Miyama, S. M., Umebayashi, T., & Nakano, T. 2000, ApJ, 543, 486
- Shakura, N. I., & Sunyaev, R. A. 1973, A&A, 24,337
- Tuthill, P. G., Monnier, J. D., & Danchi, W. C. 2001, Nature, 409, 1012

- Watson, A. M., & Stapelfeldt, K. R. 2004, *ApJ*, 602, 860
- Weidenschilling, S.J. & Cuzzi, J.N. 1993, in *Protostars and Planets III*, eds. E.H. Levy & J.I. Lunine (Tucson: University of Arizona Press), p. 1031
- Weidenschilling, S.J. 1997, *Icarus*, 127, 290
- Whitney, B. A., Wood, K., Bjorkman, J. E., & Cohen, M. 2003, *ApJ*, 598, 1079
- Whitney, B. A., Indebetouw, R., Bjorkman, J. E., & Wood, K. 2004, *ApJ*, 617, 1177
- Willacy, K., Klahr, H. H., Millar, T. J., & Henning, T. 1998, *A&A*, 338, 995
- Willacy, K., & Langer, W. D. 2000, *ApJ*, 544, 903
- Wilner, D. J., Ho, P. T. P., Kastner, J. H., & Rodríguez, L. F. 2000, *ApJ*, 534, L101
- Wilner, D. J., Bourke, T. L., Wright, C. M., Jørgensen, J. K., van Dishoeck, E. F., & Wong, T. 2003, *ApJ*, 596, 597
- Wilner, D. J., D’Alessio, P., Calvet, N., Claussen, M. J., & Hartmann, L. 2005, *ApJ*, 626, L109
- Youdin, A. N., & Shu, F. H. 2002, *ApJ*, 580, 494

Table 3. Dust to gas mass ratio

$\zeta_{small}/\zeta_{std}$	ζ_{big}/ζ_{std}
1	1
0.5	6.8
0.1	11.4
0.05	12.0
0.01	12.4
0.005	12.5
0.001	12.5
0.0005	12.5
0.0001	12.5

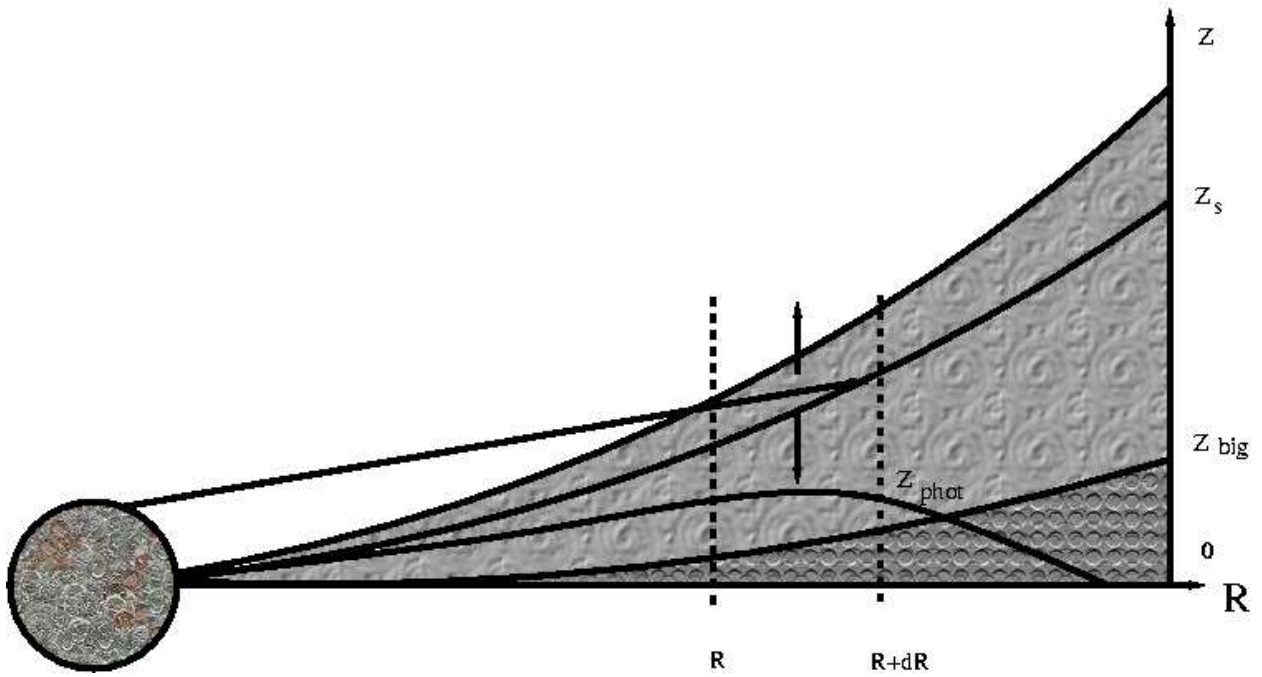


Fig. 1.— Schematic diagram of the disk geometry. Stellar radiation is intercepted by the surface $z_s(R)$. The layer above z_s is heated by direct stellar radiation, and the emission of this layer heats deeper disk regions. The disk photosphere z_{phot} is the height where the Rosseland mean optical depth is $2/3$. The outer disk can be optically thin to its own radiation, in which case it is not possible to define z_{phot} at those radii.

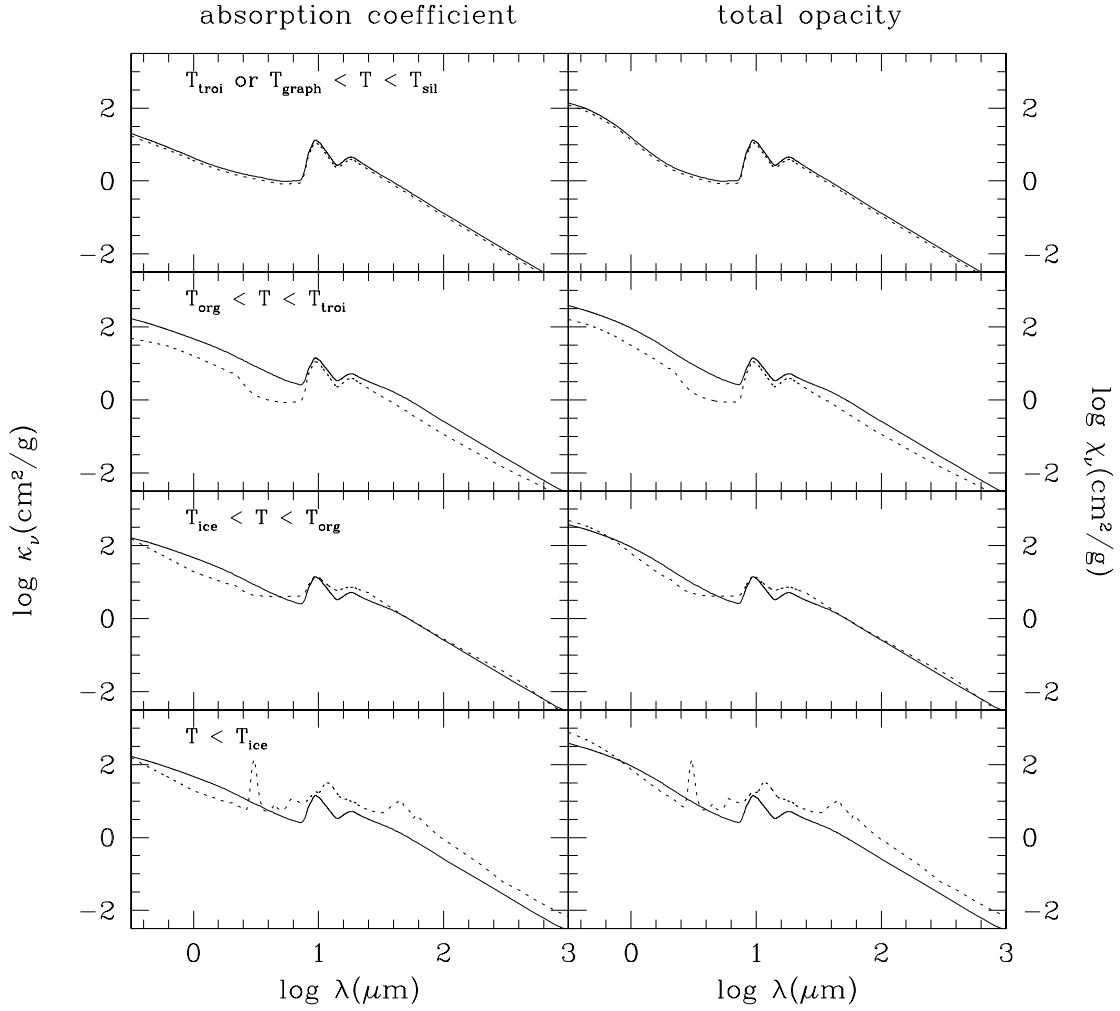


Fig. 2.— Opacity of the small grains in the upper layer. The left panels show the absorption coefficient and the right panels show the total opacity (absorption + scattering). We compare coefficients for the ISM mixture (solid line) and the P94 mixture (dotted line), for different ranges of temperature defined using the sublimation temperatures listed in Table 1

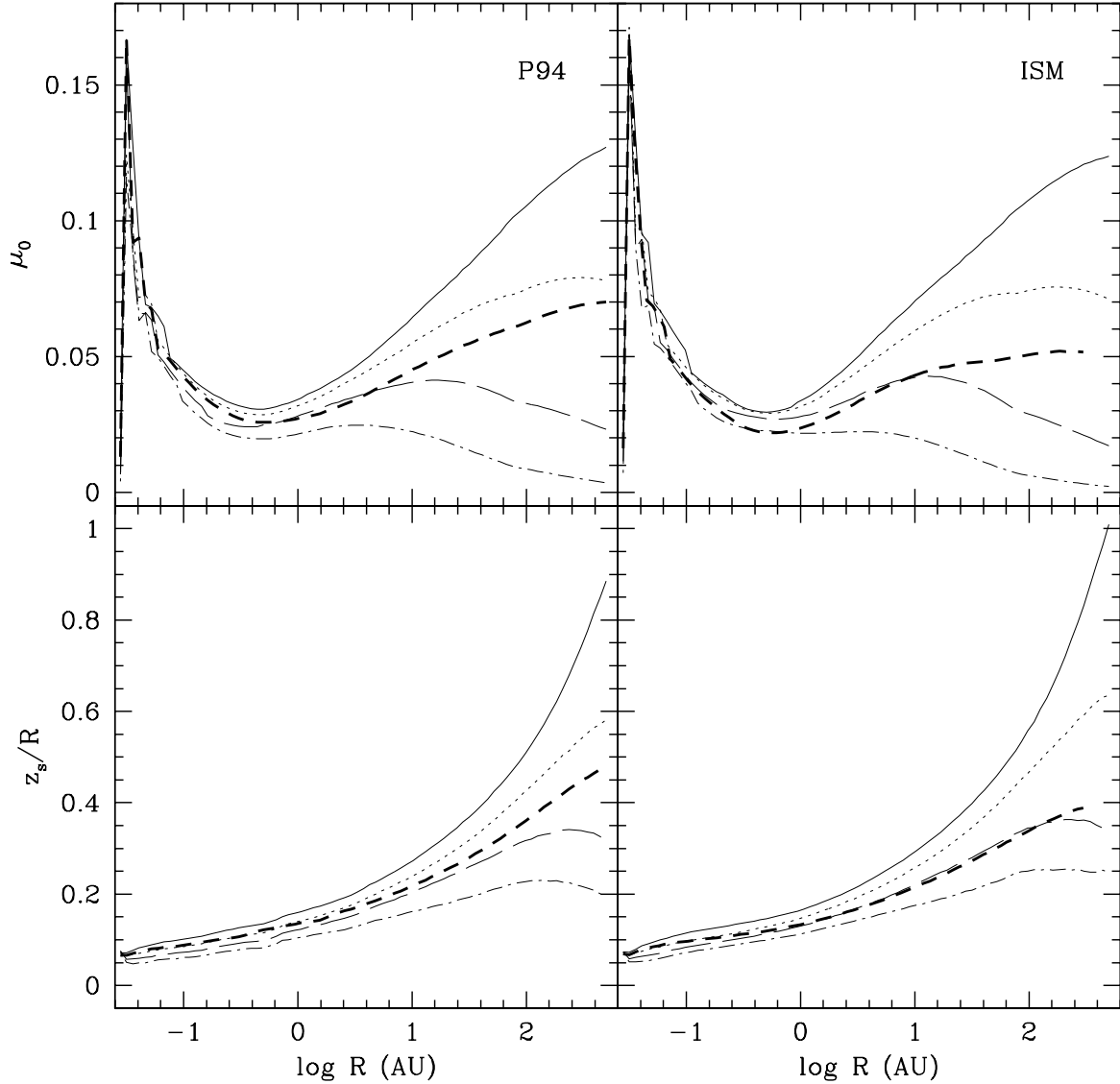


Fig. 3.— Upper panels: Cosine of the angle between the impinging stellar radiation and the normal to the disk surface. Lower panels: Height of the irradiation surface divided by radius, z_s/R , in settled disk models. In each case, the left panel corresponds to P94 dust and the right panel to ISM dust. Each curve corresponds to a different depletion of the small grain component, $\epsilon = 1$ (solid line), 0.1 (dotted line), 0.01 (long-dashed line), 0.001 (dot-dashed line). The heavy dashed line corresponds to a well mixed model with $a_{max} = 1$ mm. A model with only small grains and no depletion, is indistinguishable from the case with no depletion, $\epsilon = 1$,

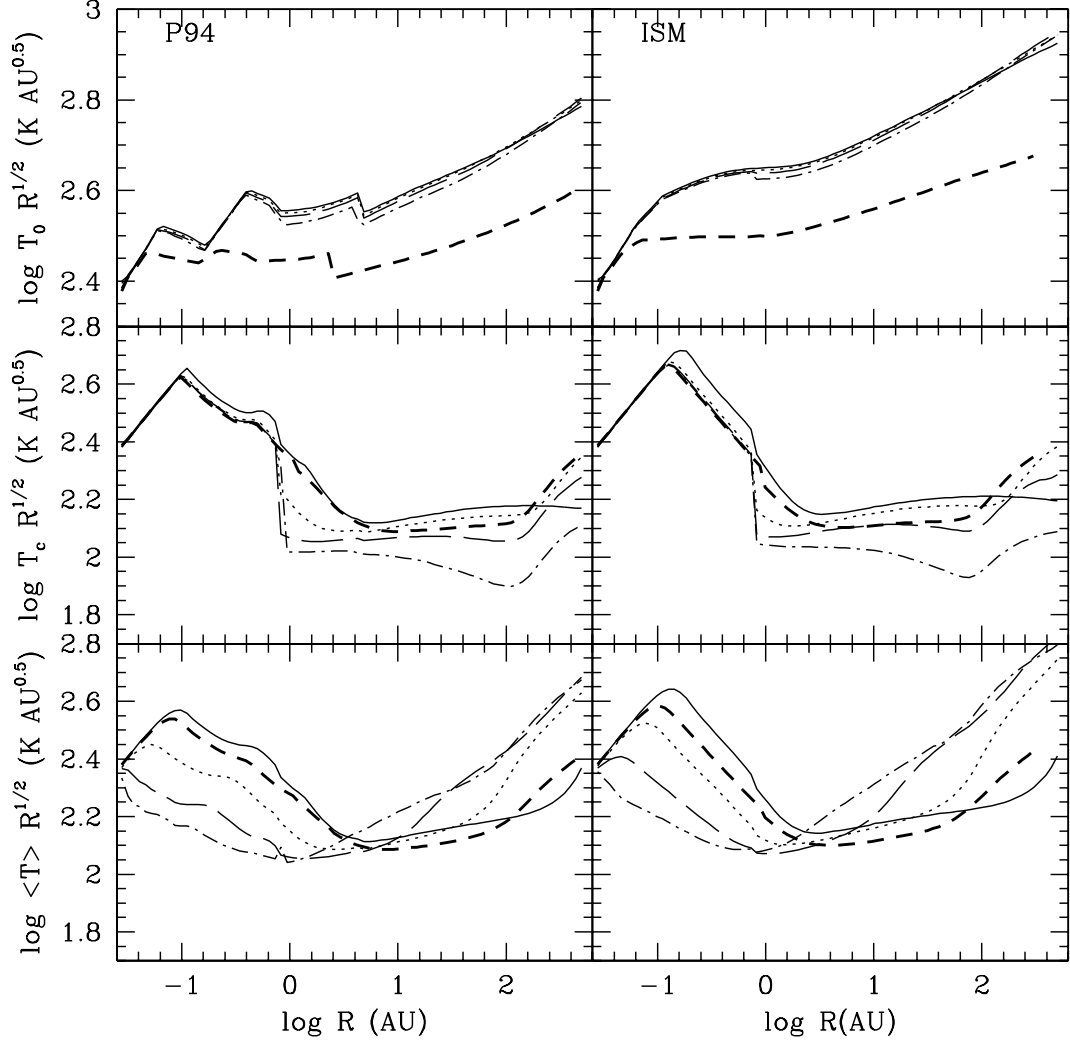


Fig. 4.— Characteristic temperatures in the disk. Upper panels: Surface temperature. Middle panels: Midplane temperature. Lower panels: Mean temperature weighted by density. To emphasize differences we plot $\log (T \times R^{1/2})$. Models are shown for two dust composition and four values of ϵ (line types as in Fig. 3).

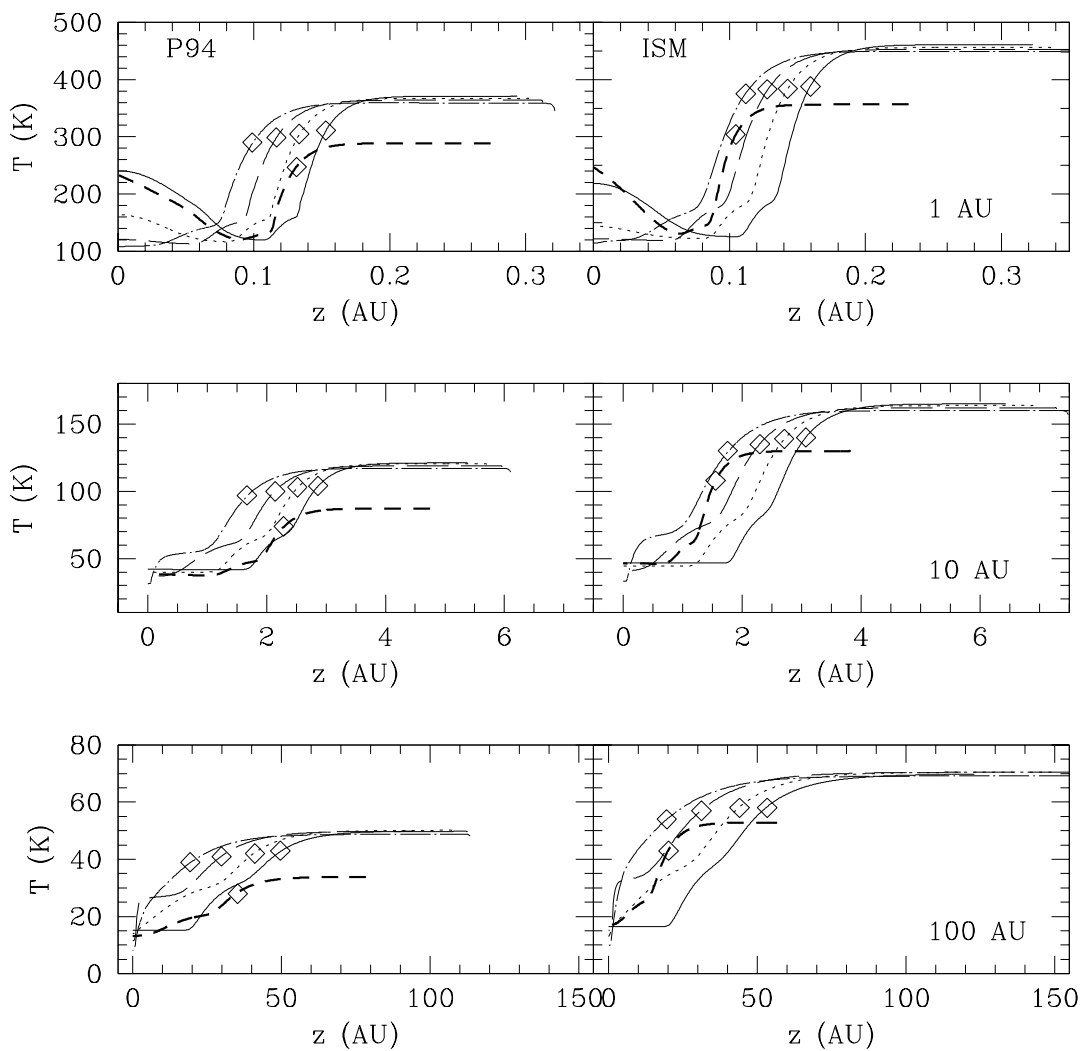


Fig. 5.— Temperature vs height at different radius. Upper panels: $R = 1$ AU. Middle panels: $R = 10$ AU. Lower panels: $R = 100$ AU. The diamonds mark the height of the irradiation surface, z_s . Models are shown for two dust composition and four values of ϵ (line types as in Fig. 3).

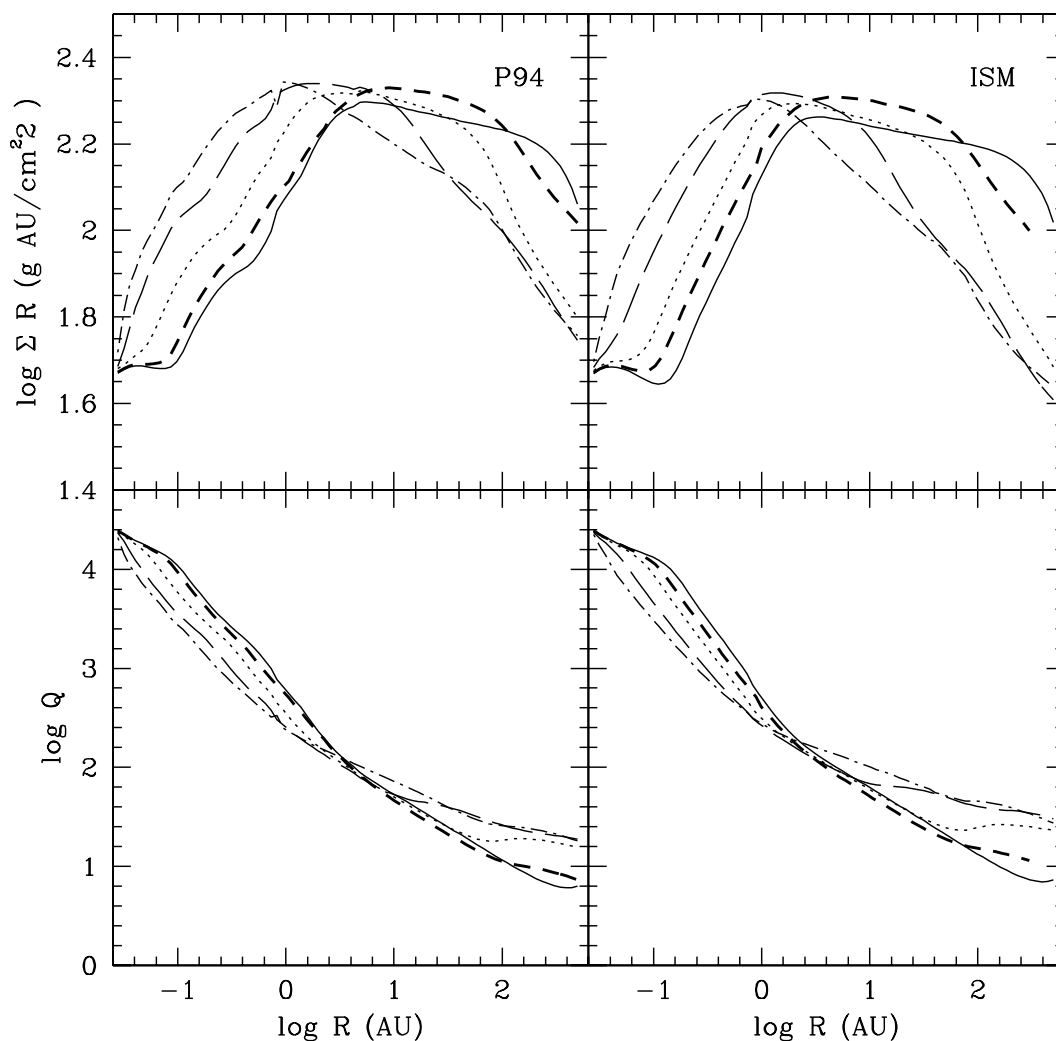


Fig. 6.— Characteristic disk properties. Upper panels: Mass surface density times radius as a function of radius. Note that the true surface density does not decline towards the central star. Lower panels: Toomre parameter evaluated at the disk midplane for the same models. A Toomre parameter $Q \lesssim 1$ indicates that the disk is gravitationally unstable. Models are shown for two dust composition and four values of ϵ (line types as in Fig. 3).

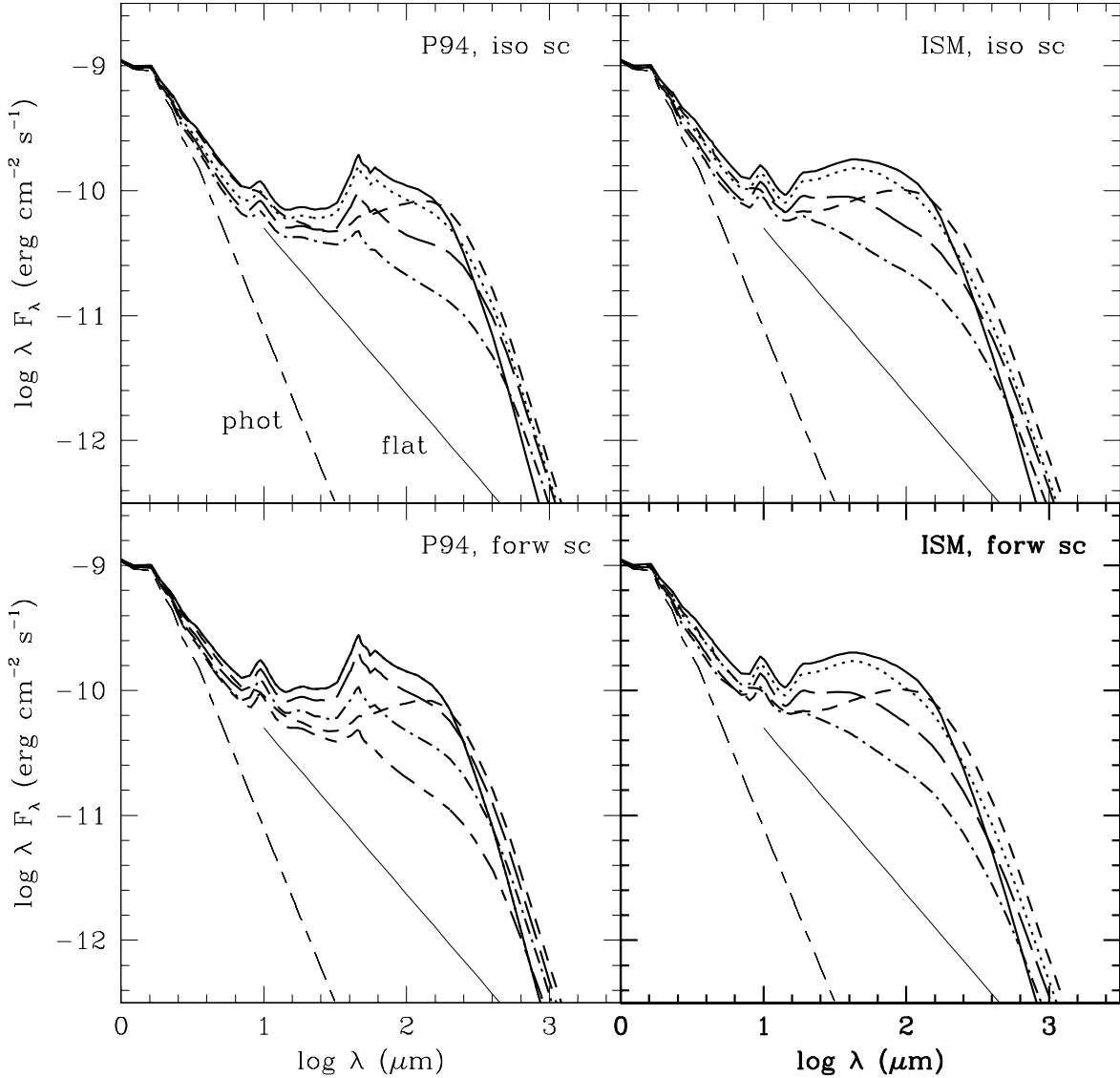


Fig. 7.— SEDs of models with ISM dust (right panels) and P94 dust (left panels), and different depletions $\epsilon = 1$ (solid line), 0.1 (dotted line), 0.01 (dot-dashed line), 0.001 (long-dashed line). For comparison, the SEDs of a well mixed models with $a_{max} = 1 \text{ mm}$ (short-dashed line) is shown. The SED for a well mixed model with $a_{max} = 0.25 \mu\text{m}$ is similar to that of the model with $\epsilon = 1$. SEDs in upper panels are calculated assuming isotropic scattering of the stellar radiation and SEDs of lower panels, assuming perfectly forward scattering. The photosphere is shown in light short-long dashed lines, and a light solid line with a slope $-4/3$, corresponding to the spectral slope of a flat disk, is shown as reference.

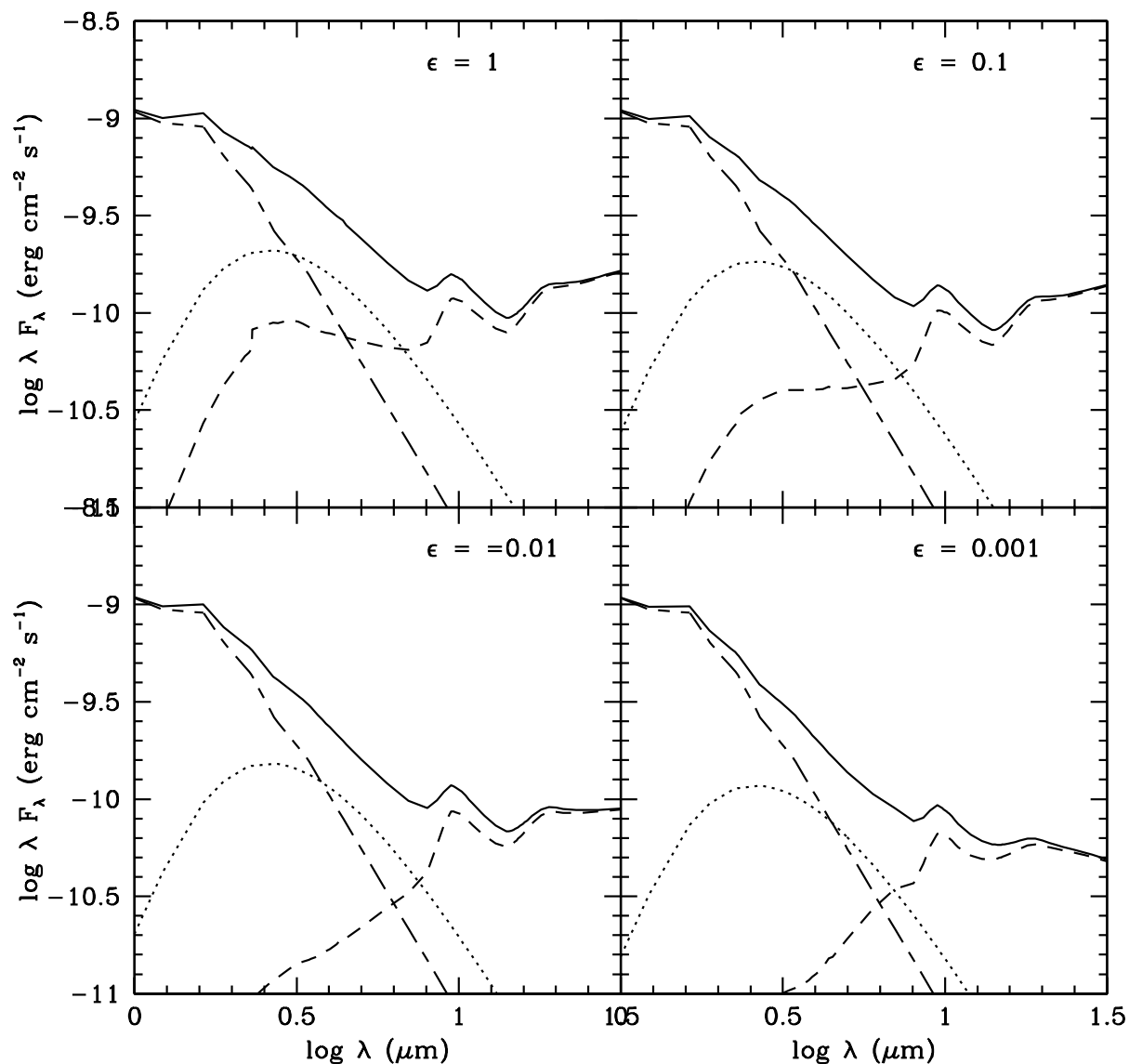


Fig. 8.— SEDs of the fiducial model with ISM dust, isotropic scattering, and four values of ϵ . The contributions of the disk (dashed line), wall at the dust destruction radius (dotted line), and photosphere (short-long dashed line) are shown separately.

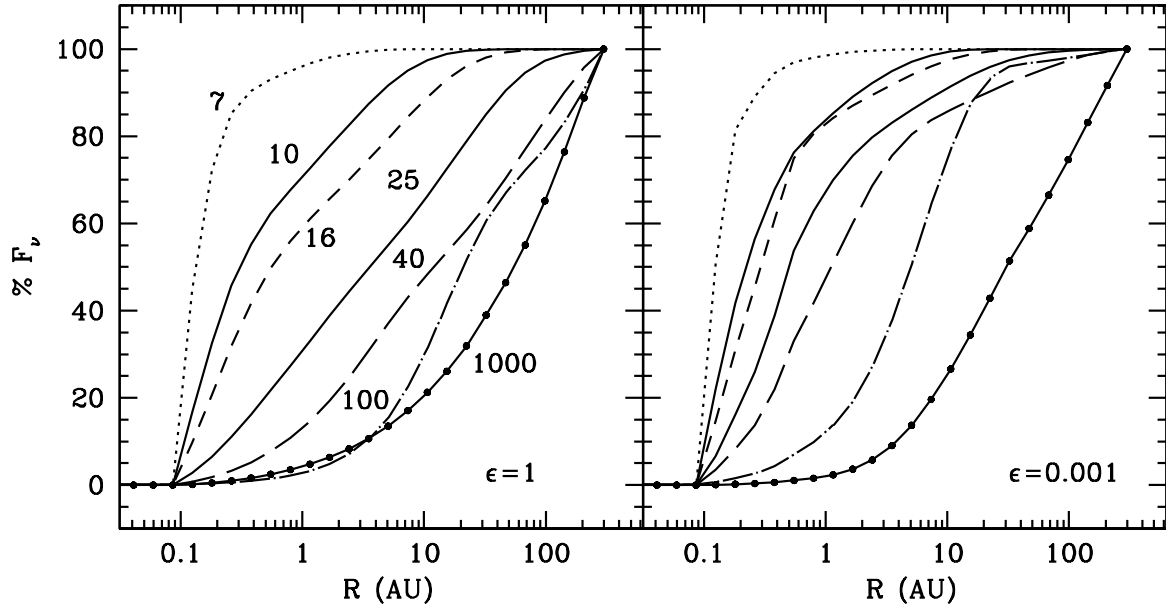


Fig. 9.— Spatial distribution of the emergent flux from the disk at different wavelengths (each curve is labeled with the wavelength in μm), for the fiducial model with $\epsilon = 1$ (left panel) and $\epsilon = 0.001$ (right panel). The models have ISM dust and isotropic scattering and the disk radius is 100 AU.

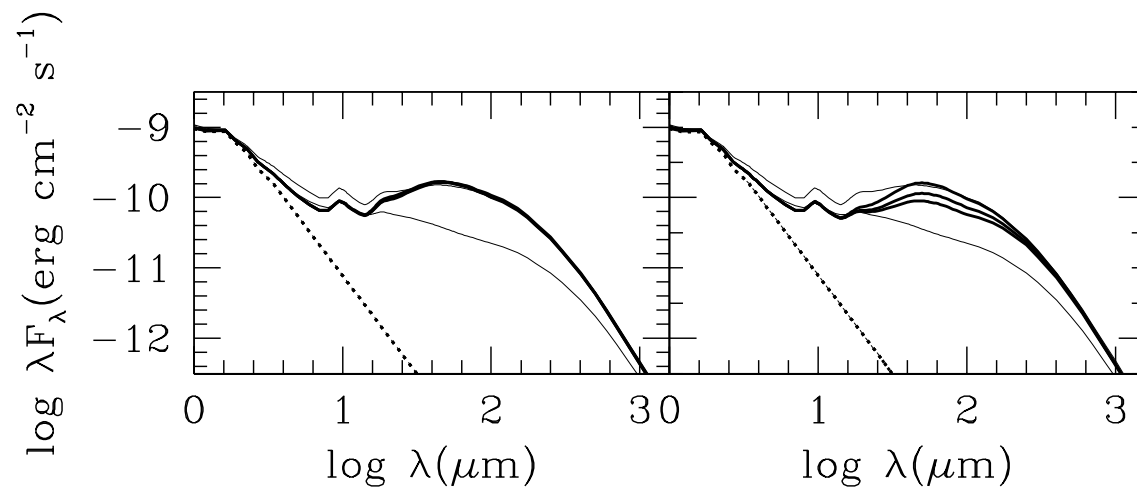


Fig. 10.— SEDs of models with $\epsilon(R)$. Models with $\epsilon_1 = 0.01$ and $\epsilon_2 = 0.1$, spanning different regions in the disk. Left: $R_1 = 10$ AU and $R_2 = 50, 75,$ and 90 AU, thick lines from top to bottom. Right: $R_1 = 50$ AU and $R_2 = 75, 100,$ and 200 AU, thick lines from top to bottom. For comparison, in the two panels we show SEDs of models with constant $\epsilon = 0.1$ and 0.01 (upper and lower light solid lines).

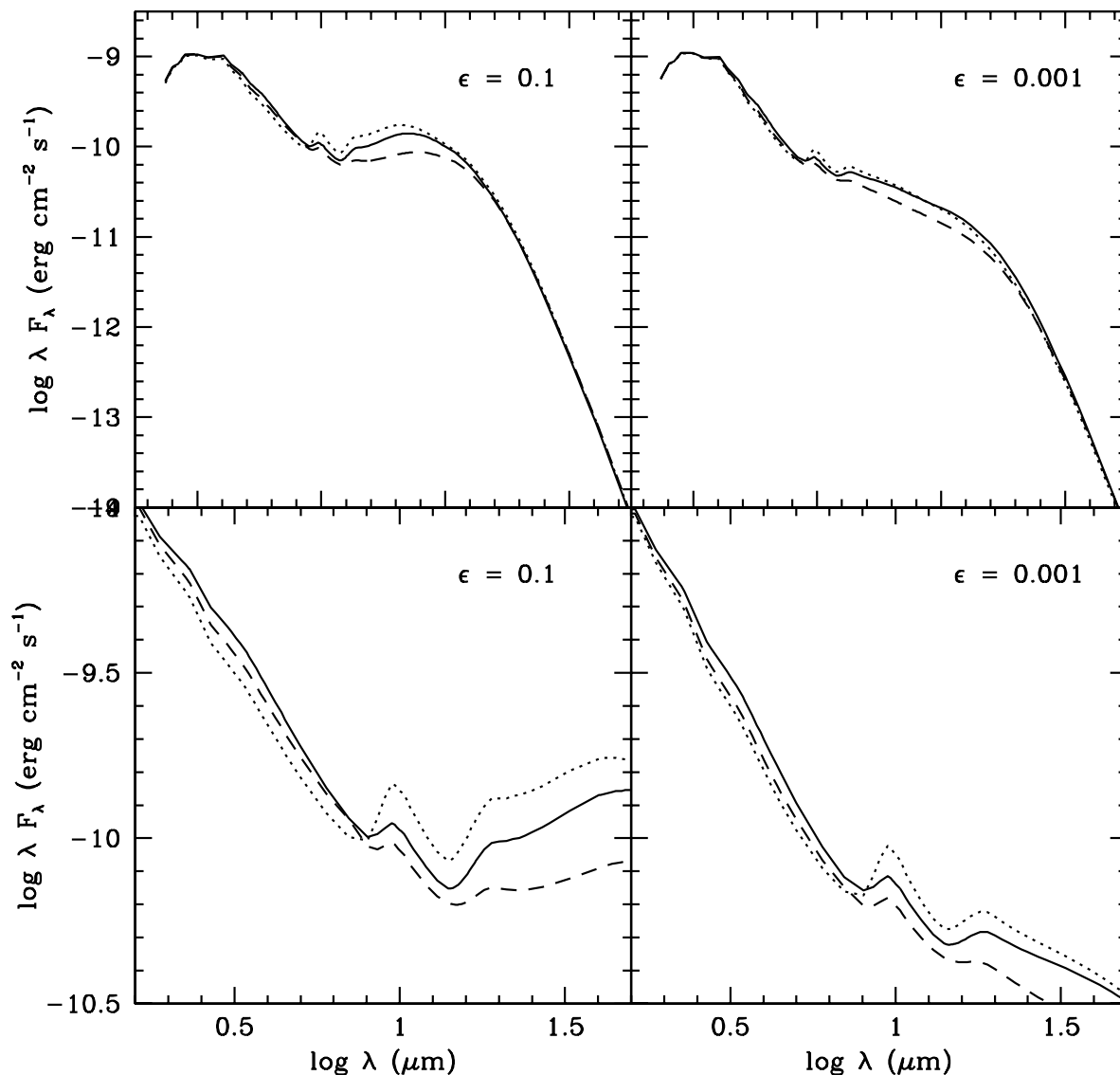


Fig. 11.— SEDs of the fiducial model showing the dependence on the grain size distribution in the upper layers. The models are for ISM dust and isotropic scattering, for $\epsilon = 0.1$ (left panels) and 0.001 (right panels), and for three values is a_{max} for the dust grains in the upper layers, $a_{max} = 0.05 \mu\text{m}$ (dotted lines), $1 \mu\text{m}$ (solid lines), and $10 \mu\text{m}$ (dashed lines). The lower panels show the region of silicate features in more detail.

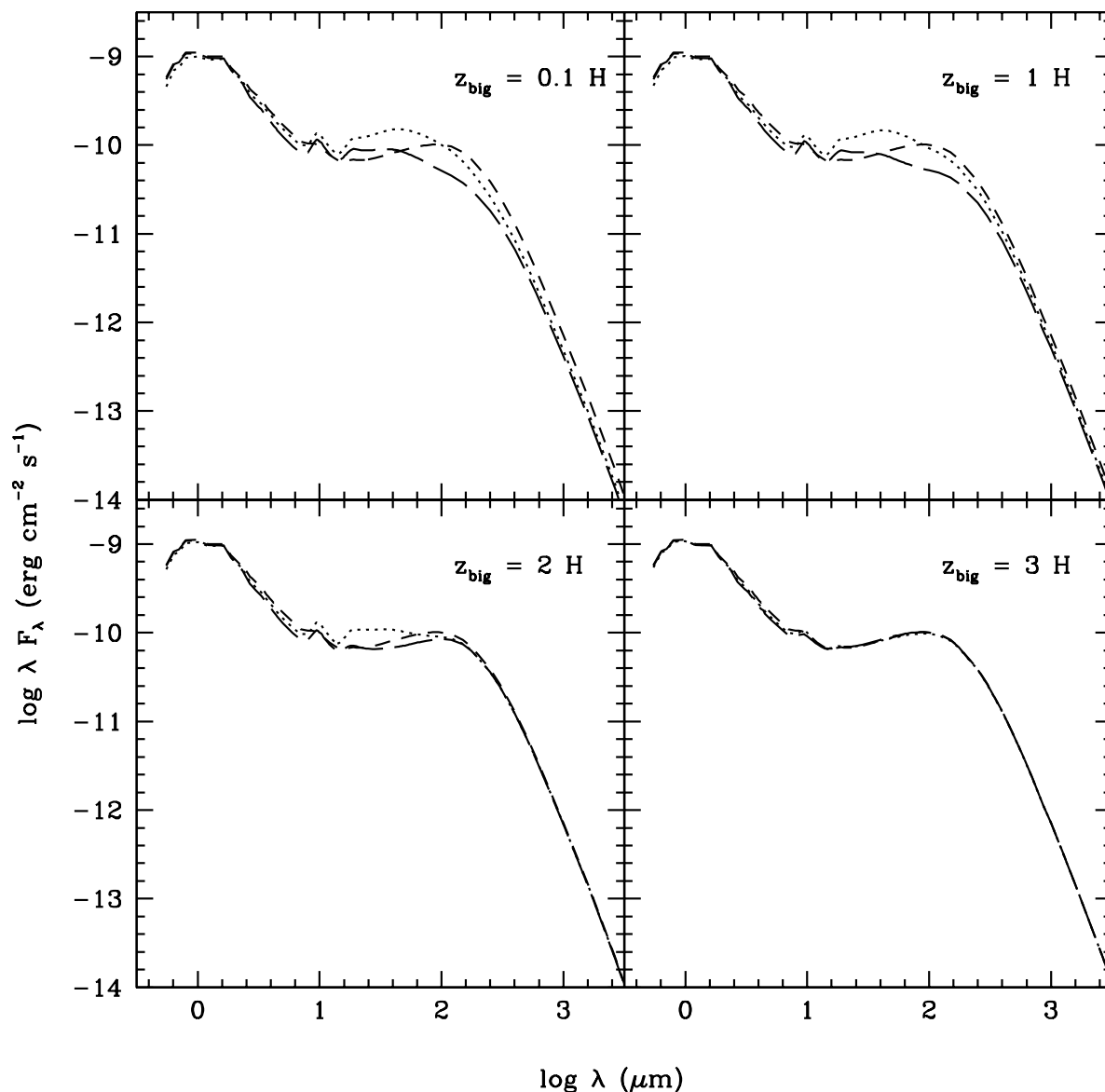


Fig. 12.— SEDs of the fiducial model showing the dependence on the height of the big grains layer. The models are for ISM dust and isotropic scattering, for $\epsilon = 0.1$ (dotted line), and 0.01 (dashed line). and for $z_{big} = 0.1, 1, 2,$ and $3 H$, where H is the scale height. Also the SED of the well mixed model with $a_{max} = 1$ mm and $\epsilon = 1$ is shown in each panel (thick dashed line) for reference.

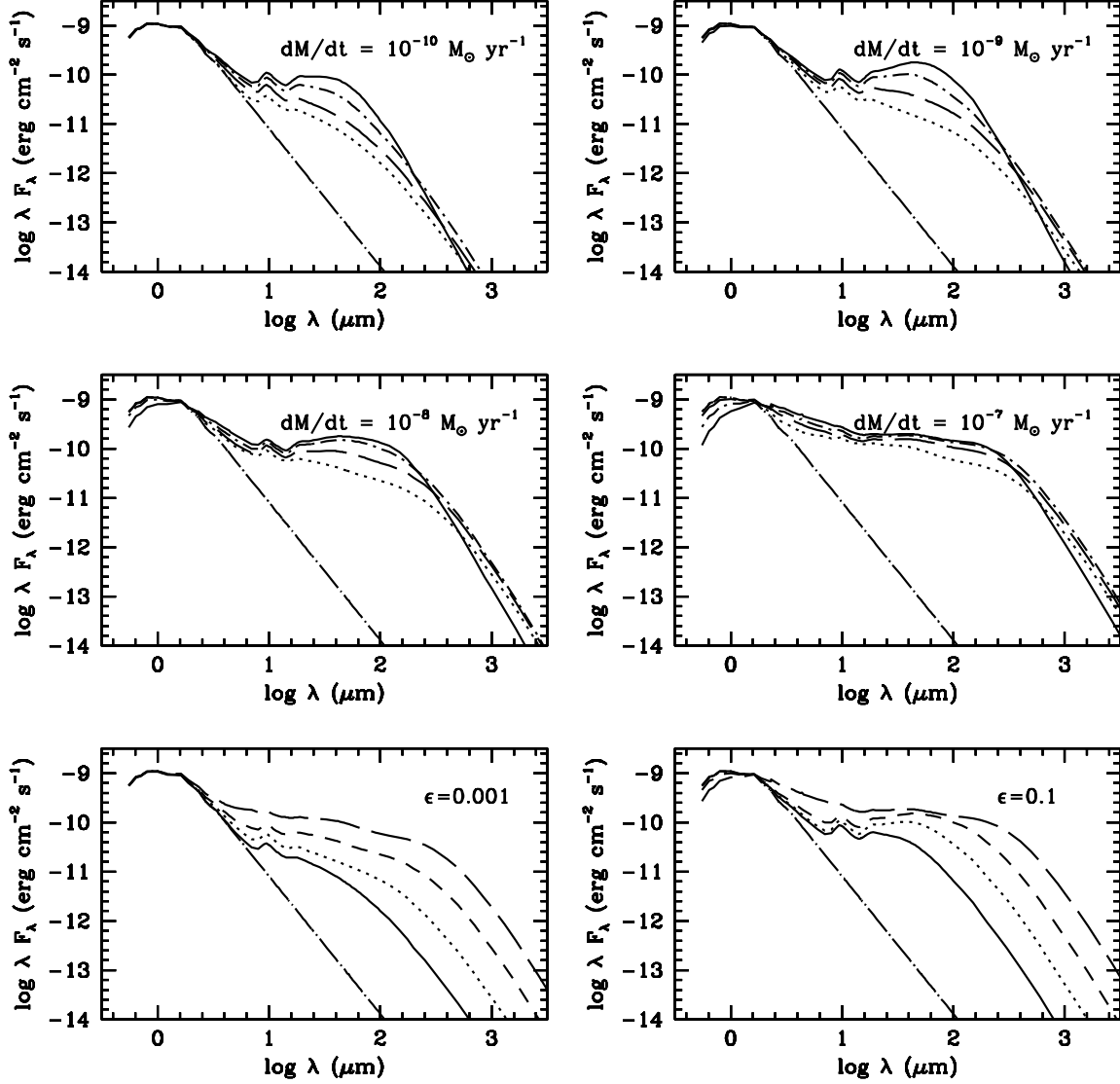


Fig. 13.— SEDs of fiducial disk model with ISM dust, varying the mass accretion rate. Each of the four upper panels correspond each one to a different value of \dot{M} , indicated in the panel. Each curve correspond to different ϵ : 0.001 (dotted line), 0.01 (long dashed line), 0.1 (short dashed line) and 1 (solid line). The two lower panels show a selection of the same models for fixed ϵ , varying the mass accretion rate: $\dot{M} = 10^{-10}$ (solid), 10^{-9} (dotted), 10^{-8} (dashed) and $10^{-7} M_{\odot} \text{ yr}^{-1}$ (long dashed line)

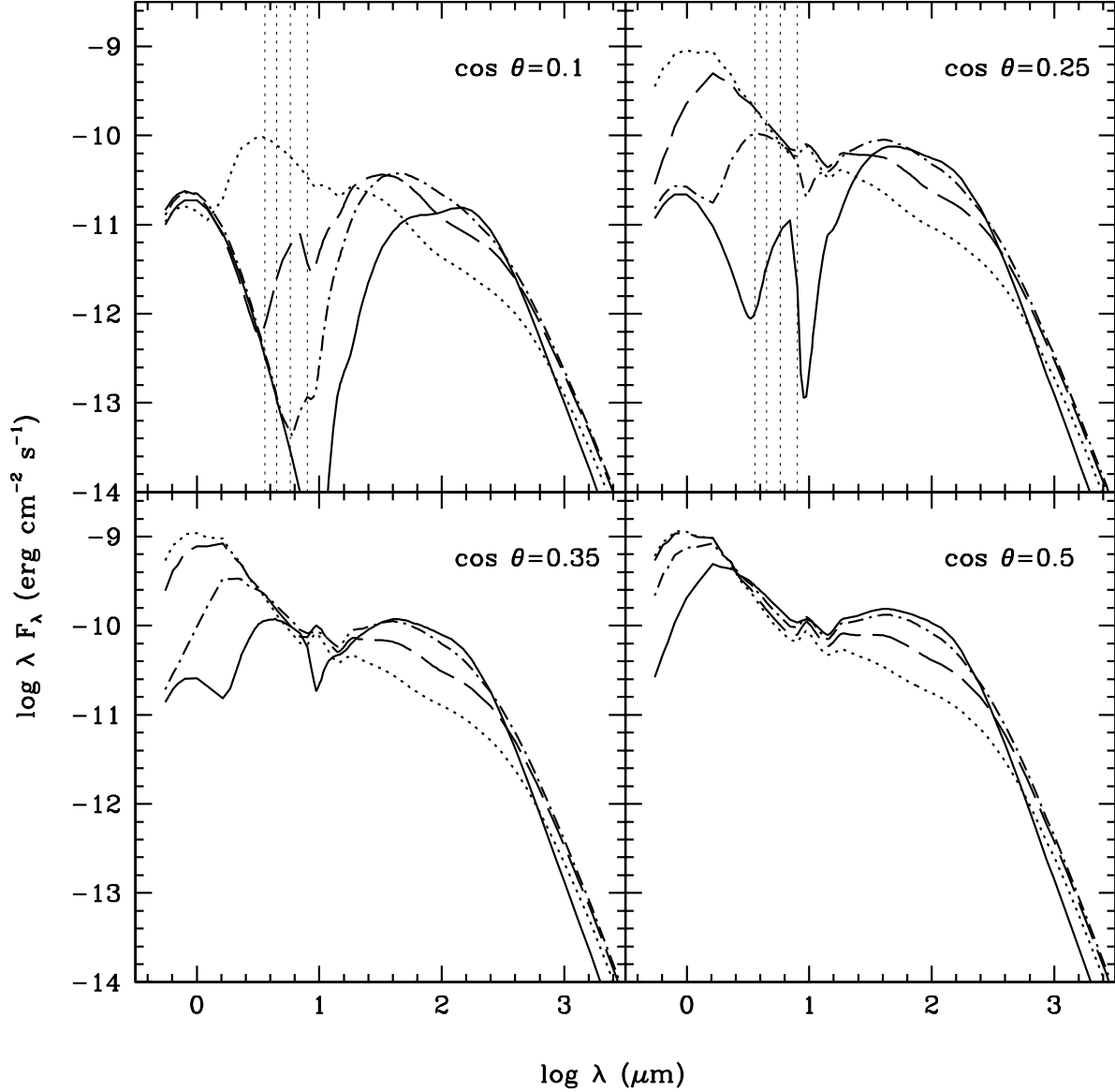


Fig. 14.— SEDs of the fiducial disk model with ISM dust and isotropic scattering with its axis inclined to $\cos i = 0.1, 0.25, 0.35$ and 0.5 ($i = 84, 75.5, 69.5$ and 60°) with respect to the line of sight, and, four values of the settling parameter: $\epsilon = 1$ (solid), 0.1 (short-dashed), 0.01 (long-dashed) and 0.001 (dotted). The dotted lines in the upper panel indicate the central wavelengths of the IRAC bands.

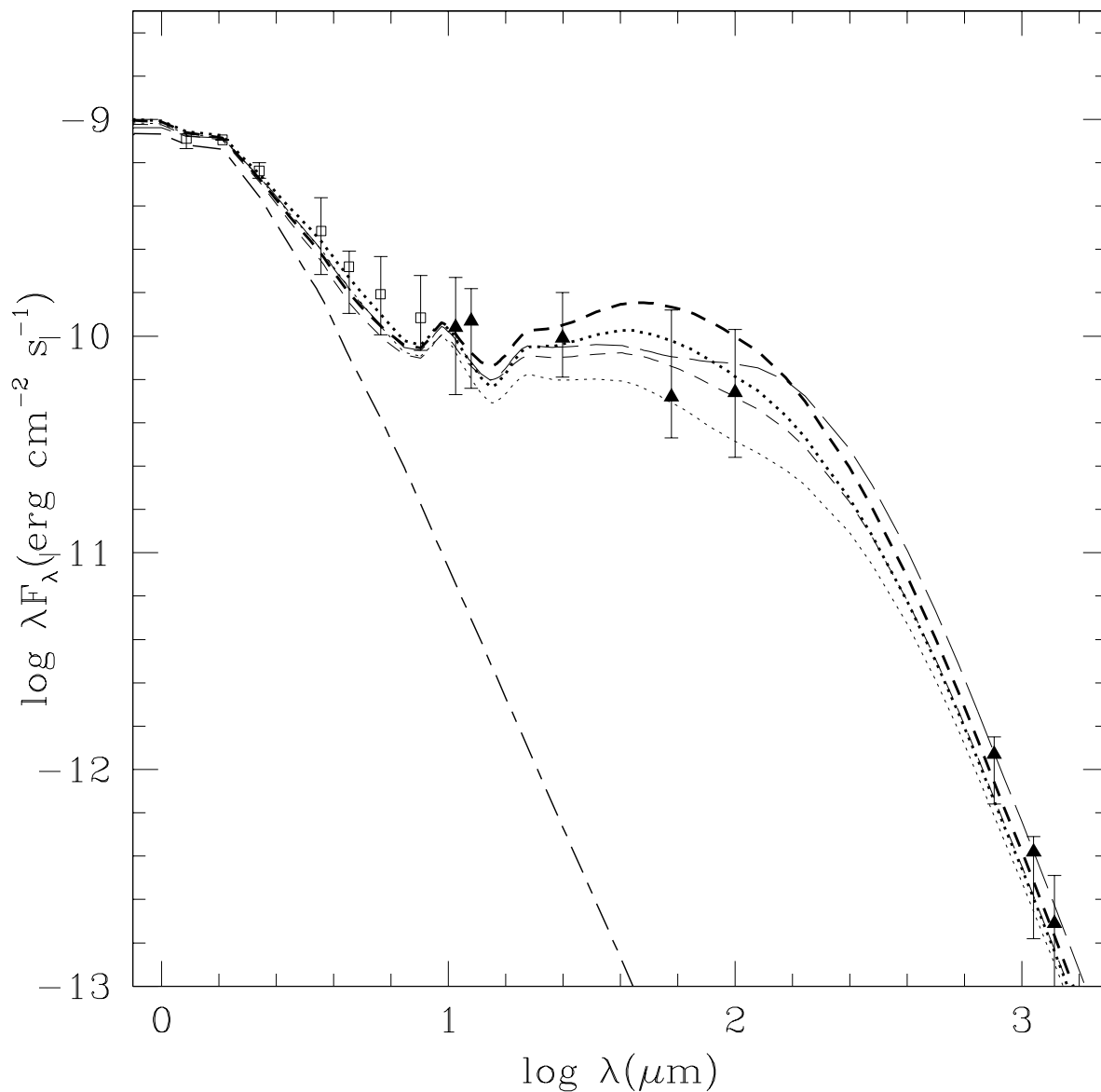


Fig. 15.— SEDs of the fiducial model with ISM dust, for $\epsilon = 0.1$ (heavy lines) and $\epsilon = 0.01$ (light lines), and for two inclinations: $\mu = 0.5$ (60° , solid lines) and $\mu = 0.87$ (30° , dashed lines). The lower dot-short line indicates the photosphere. A model with $\epsilon = 0.1$ and $z_{big} = 2$ H from Figure 12 is also shown (long-dash line). The open squares represent the median SED of CTTS observed with IRAC (Hartmann et al. 2005), the triangles are the median SED in Taurus from D’Alessio et al. (1999). In each case, the error bars correspond to the quartiles.

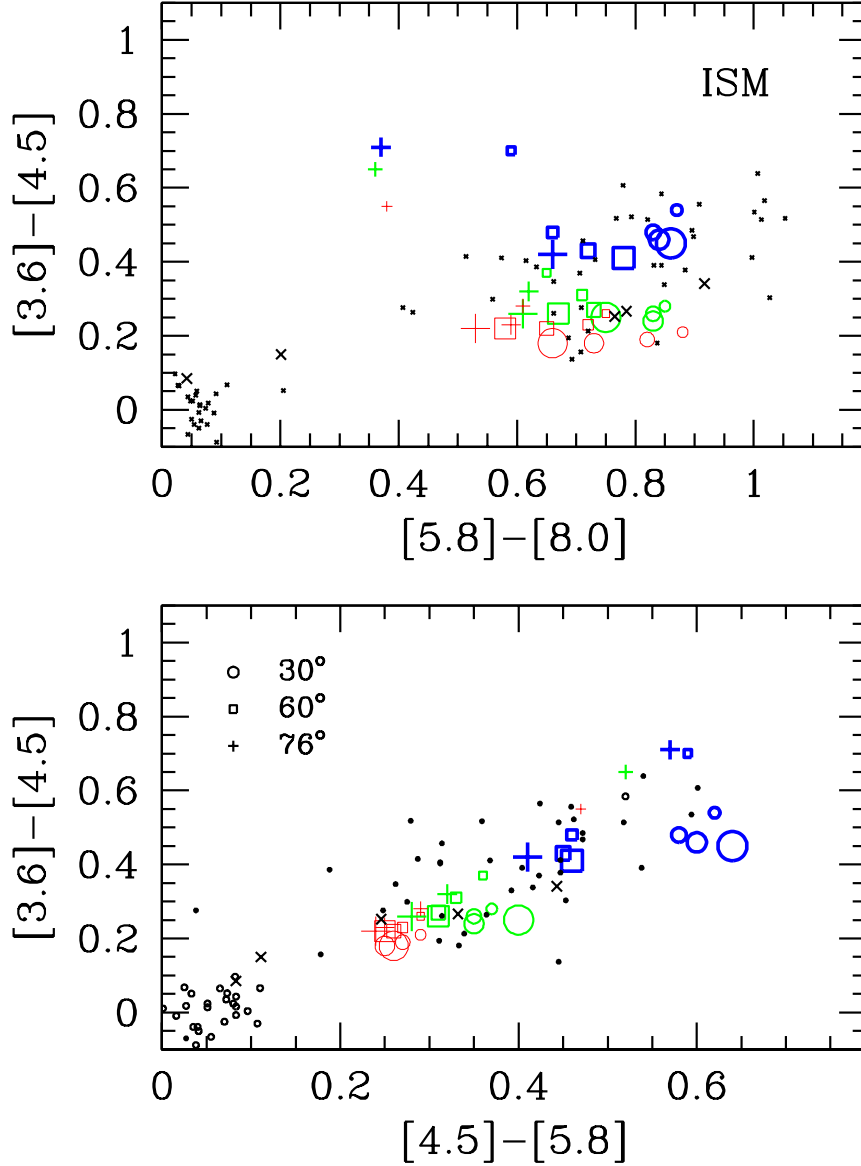


Fig. 16.— Comparison of predicted and observed IRAC colors for Classical T Tauri stars in Taurus. The data is taken from Hartmann et al. (2005) and are shown as small solid dots. Open small circles are weak T Tauri stars. Model colors are shown for three mass accretion rates: $10^{-7}M_{\odot}\text{yr}^{-1}$ (heavy weight), $10^{-8}M_{\odot}\text{yr}^{-1}$ (medium weight), and $10^{-9}M_{\odot}\text{yr}^{-1}$ (light weight), four values of the settling parameter $\epsilon = 1$ (smallest symbols), 0.1, 0.01, and 0.001 (largest symbols), and three values of inclination $\cos i = 0.24$ ($i = 76^\circ$, crosses), $\cos i = 0.5$ ($i = 60^\circ$, open squares), and $\cos i = 0.87$ ($i = 30^\circ$, open circles).

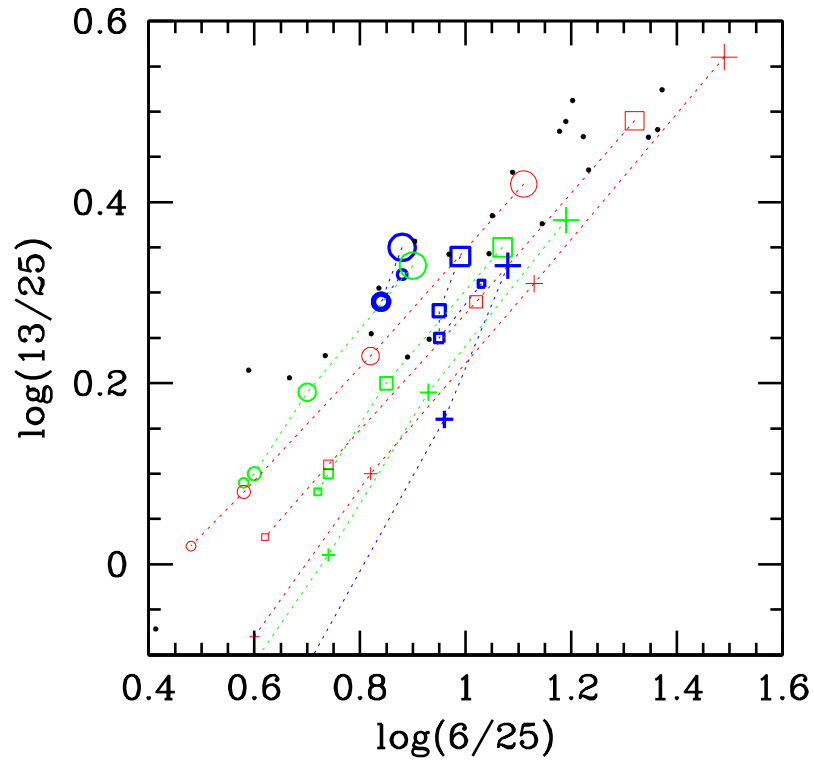


Fig. 17.— Comparison of model predictions with mid-IR indices derived from IRS spectra for CTTS in Taurus from Furlan et al. (2005a,b). Observations are shown in black small dots. Model symbols as in Fig. 16. For guidance, dotted lines connect models with same inclination.

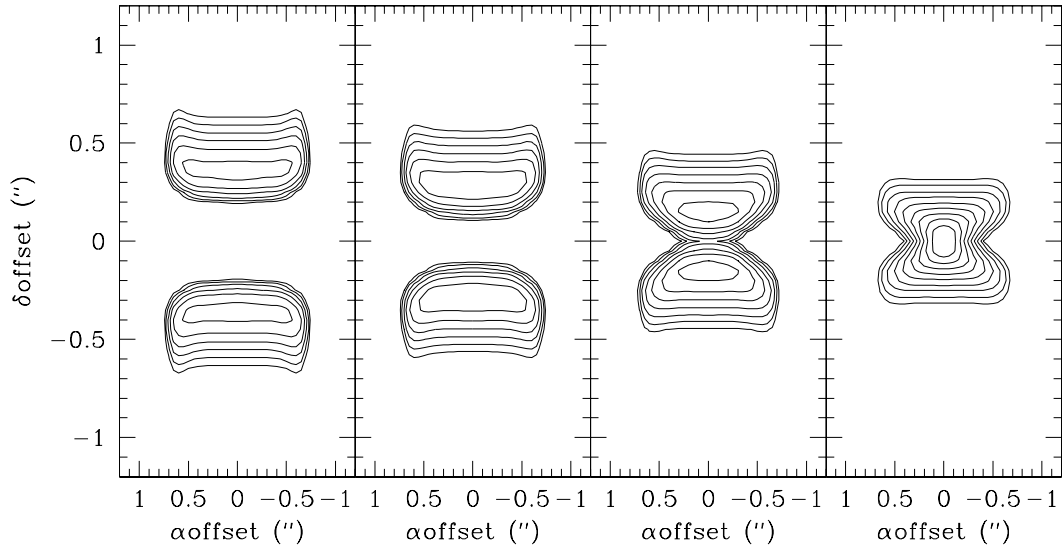


Fig. 18.— Images of edge-on disk models with different depletions at $\lambda = 0.8 \mu m$, convolving with a 0.1 '' Gaussian beam. From left to right, $\epsilon = 1, 0.1, 0.01, 0.001$. The asymmetry factor is self-consistently calculated for the dust mixture ($g = 0.33$). The plots have the same isocontours, with a maximum of 0.5 mJy/beam and a minimum of 0.005 mJy/beam .

